BMP-signaling in the intestinal epithelium drives a critical feedback loop to restrain IL-13-driven tuft cell hyperplasia

Håvard T. Lindholm[1,+*], Naveen Parmar[1,+], Claire Drurey[2], Marta Campillo Poveda[2], Pia Vornewald[1], Jenny Ostrop[1], Alberto Díez-Sanchez[1], Rick M. Maizels[2], and Menno J. Oudhoff[1,*]

[1]CEMIR – Centre of Molecular Inflammation Research, Department of Clinical and Molecular Medicine, NTNU – Norwegian University of Science and Technology, 7491 Trondheim, Norway

[2]Wellcome Centre for Integrative Parasitology, Institute of Infection, Immunology and Inflammation, University of Glasgow, G12 8TA Glasgow, United Kingdom.

[+]these authors contributed equally to this work

[*]corresponding authors: havard.t.lindholm@ntnu.no and menno.oudhoff@ntnu.no

Abstract

The intestinal tract is a common site for different types of infections including viruses, bacteria, and helminths, each requiring specific modes of immune defense. The intestinal epithelium has a pivotal role in both immune initiation and effector stages, which are coordinated by immune-type specific cytokines such as IFNγ, IL-13 and IL-22. Here, we study intestinal epithelial immune responses using organoid image analysis based on a convolutional neural network, transcriptomic analysis, and *in vivo* infection models. We find that IL-22 and IL-13 both induce genes associated with goblet cells, but their phenotypes are dichotomous. Moreover, only IL-13 driven goblet cells are associated with classical NOTCH signaling. We further show that IL-13 induces BMP signaling, which acts in a negative feedback loop in immune type 2 driven tuft cell hyperplasia. This is associated with inhibiting *Sox4* expression to putatively limit the tuft progenitor population. Blocking BMP signaling with the ALK2 inhibitor DMH1 interrupts the feedback loop, resulting in greater tuft cell numbers both *in vitro* and *in vivo* after infection with *Nippostrongylus brasiliensis*. Taken together, these novel aspects of cytokine effector responses reveal an unexpected and critical role for BMP signaling in type 2 immunity, which can be exploited to tailor epithelial immune responses.

Introduction

Gut infections remain a common threat for patients and are an immense burden on health systems worldwide (*1*). Resistance to intestinal pathogens relies on the capacity of the immune system to mount an appropriate response. For example, one requires a different type of response to intracellular viruses compared to extracellular pathogens including bacteria or parasites. Cytokines are key participants in polarizing the immune response by altering the cellular composition and state. Innate lymphoid cells (ILCs) are tissue resident immune cells which are early responders to infections and create a local cytokine environment. ILCs are classically divided into three groups and secrete IFNγ (group 1), IL-13 (group 2), and IL-22 (group 3), and which ILC subtype is dominant depends on the pathogenic challenge (*2*).

In addition to defining the immune landscape, cytokines directly affect intestinal epithelial cells (IECs) to drive immune-type specific responses (*3*). The intestinal epithelium consists of a single layer of cells and is responsible both for taking up nutrients as well as providing a protective barrier. One of the hallmarks of IECs is their rapid turnover (3-5 days), which allows for prompt cellular responses, for example, to expand goblet cells which can produce protective mucus. This plasticity of IECs makes them particularly well-suited to defend against pathogens (*4*).

In addition to responding to immune cues, the epithelium can also be involved in tailoring immune responses. For example, tuft cells, which are important for defending against parasitic helminths, are the main source of IL-25 to control ILC2 populations both in homeostasis and upon helminth infection (*5–7*). As tuft cells rapidly expand upon exposure to type 2 cytokines, they exemplify both how the intestinal epithelium changes upon an immune response and how it can partake in shaping it. Of note, tuft cells are not only important in immunity to helminth infections; activation of tuft cells by succinate is protective in a murine model of colitis, and reduced tuft cell numbers are found in patients with Crohn's disease that have more severe inflammation (*8*). Thus, tuft cells have been gaining interest as important regulators of intestinal diseases (*9*), and the discovery of regulatory mechanisms could have clinical ramifications.

Intestinal organoids are self-organizing structures that are useful to study epithelial (stem) cell

biology (*10*). They are particularly instructive to identify epithelial-intrinsic responses as they lack any other cell type normally present *in vivo*, such as fibroblasts. This also means their culture medium requires addition of growth factors normally supplied by fibroblasts, such as those that target pathways such as WNT and BMP. In addition, organoid cultures come with challenges as most metrics cannot capture the complexity of these large multicellular structures. To capture this complexity, a study used single cell RNA sequencing (scRNA-seq) to systemically compare single cell responses to cytokines of the three immune environments (*3*). However, there are still many unclear aspects to how cytokines induce epithelial responses, especially mechanistically. Here we combine quantitative imaging with bulk RNA-seq to define how cytokines intercept developmental pathways to instruct epithelial differentiation and maturation. Most prominently, we identify a feedback loop by which IL-13 induced tuft cell hyperplasia is self-limiting in a BMP-dependent manner, and confirm this in a murine helminth infection model using *N. Brasiliensis*.

Results

IFNγ, IL-13, and IL-22 uniquely affect organoid growth and morphology

Intestinal organoids grow as a morphologically heterogeneous population, where a fraction of organoids grow as immature "spheroids" and the rest form mature "budding" organoids. *Lgr5+* stem cells and Paneth cells are found in the buds in budding organoids (mimicking crypts) while spheroids consist of less differentiated, proliferating cells (*11*). Building on our recent work on organoid segmentation (*12*), we here developed an automated image analysis pipeline that segments organoid objects from the background and subsequently classifies them into "spheroid" or "budding" categories based on a convolutional neural network (Fig. 1A). This includes an optional manual correction step for organoids that were difficult to automatically segment or classify (Fig. S1A). Comparing manually verified with automatically classified and segmented images had a good correlation in analysis of >20,000 organoids (Fig. S1B). Expectedly, we find that in time the number of spheroids decrease and appear darker in appearance, confirming that our systematic

approach captures what is observed visually (Fig. S1C,D,E).

To mimic different types of immune responses, we treated organoids with key cytokines IFNγ, IL-13, or IL-22. As was previously found (*13*, *14*), long term IL-22 or IFNγ treatment ultimately leads to organoid disintegration (Fig. S1F). At an earlier time point (day 2), this is characterized by a darker appearance, reduced percentage of spheroids, and an increased percentage of budding organoids (Fig. 1B,C and S1G). In contrast, a population of IL-13 treated organoids form large spheroids at day 2 (Fig. 1C and S1G).

Tuft cells are a specific epithelial cell type involved in type 2 immunity, and induced by IL-13 (*6*, *7*). Tuft cells in organoids share the characteristic shape and F-actin brush with their *in vivo* counterparts (Fig. S2A) (*15*). We next combined our classification setup with confocal imaging to automatically quantify tuft cells in organoid subtypes. This configuration allows for classification and counting of tuft cells in hundreds of organoids and supports both automatic estimates of tuft cell number and a more accurate manually curated count (Fig. S2B). Indeed, we find that tuft cells primarily appear in budding organoids both in control and IL-13-treated conditions (Fig. S2C,D,E). Together, these data show that classification of organoids combined with confocal imaging provides a tractable measure of epithelial cellular responses.

IFNγ, IL-13, and IL-22 uniquely affect RNA expression in organoids in a manner aligned to *in vivo* infection profiles

To assess in detail how IFNγ, IL-13, and IL-22 affect intestinal epithelial cells we performed bulk RNA-seq on organoids treated with indicated cytokines for 24 hours compared to untreated controls (Fig. 1D). The different cytokines showed up-regulation of unique genes that grouped separately in a PCA plot, and each cytokine induced different GO-terms, highlighting the different effector responses required to each type of immune response (Fig. 1E,F, S3A-D).

To investigate to what degree cytokines control the epithelial response *in vivo*, we performed RNA-seq on intestinal epithelium from mice infected with *Nippostrongylus brasiliensis* or *Citrobacter rodentium*, which are classical intestinal infection models for a parasitic and extracellular bac-

terial infection respectively (Fig. S4A). Intestinal epithelium infected with *N. brasiliensis* did show the expected induction of tuft cells (Fig. S4C,D,E) and had up-regulation of GO terms associated with wound healing (Fig. S4F). Intestinal epithelium infected with *C. rodentium* had up-regulation of GO-terms associated with inflammatory response (Fig. S4G). We found that epithelium from duodenum isolated from *N. brasiliensis* infected mice was similar to IL-13 treated-organoids (Fig. 1G). In contrast, colonic epithelium isolated from *C. rodentium* infected mice aligned with IL-22- and IFNγ-treated organoids using gene set enrichment analysis (GSEA) (Fig. 1G). A caveat to the analysis of *C. rodentium* analysis is that this epithelium is isolated from colon and not small intestine. The correlation with IL-13 induced genes in *N. brasiliensis* infected epithelium and IL-22 induced genes in *C. rodentium* infected intestinal epithelium aligns with the standard model of the involvement of these cytokines in specific immune responses and indicates that treating intestinal organoids with cytokines provide a relevant model to, in part, mimic *in vivo* epithelial responses.

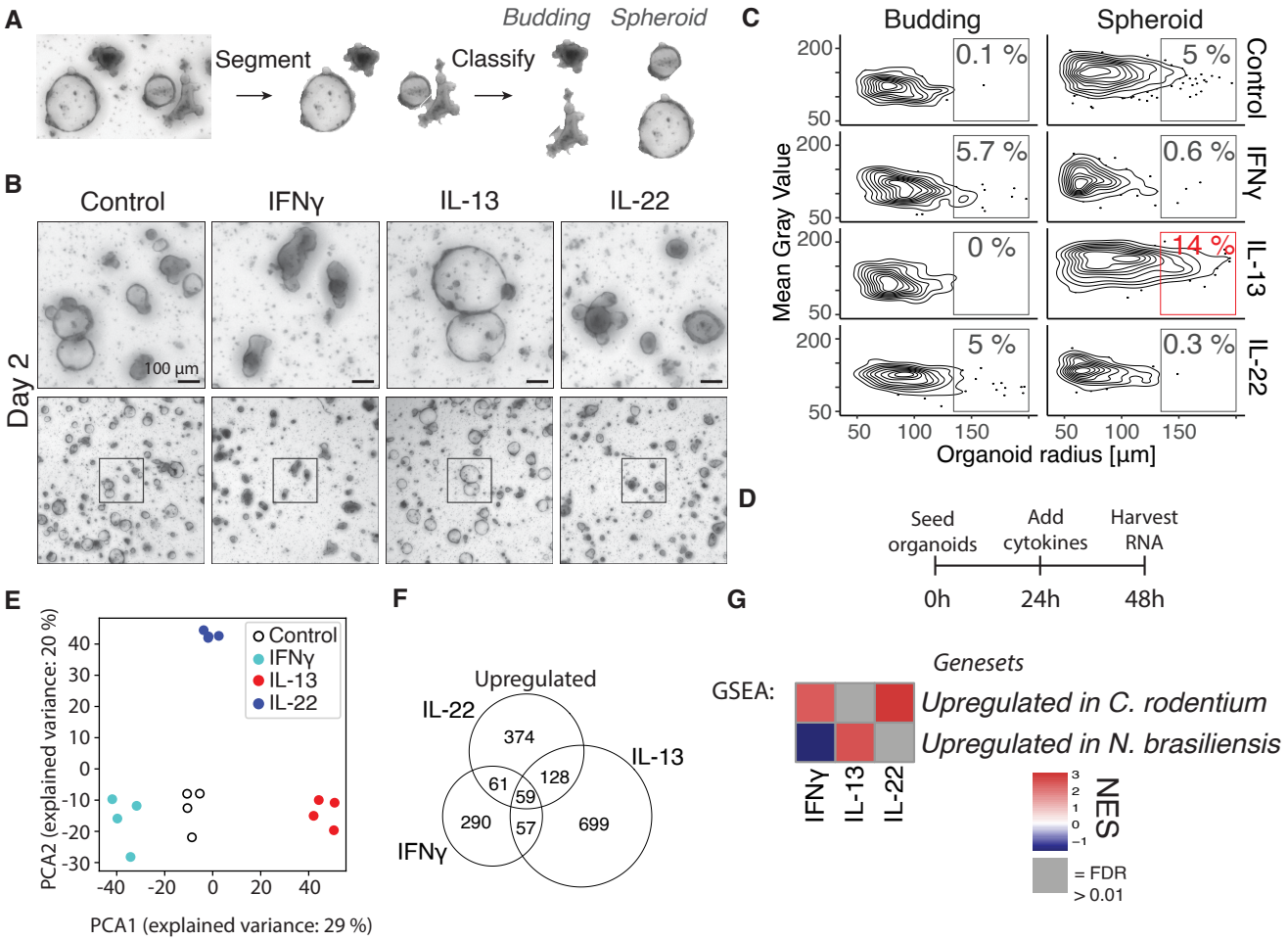

Figure 1: Cytokines modify development of small intestinal epithelium in a cytokine-specific manner and correspond to *in vivo* infection models. **A**, Image segmentation and classification of organoid images. **B**, Bright field images of small intestinal organoids treated with 10 ng/mL cytokine since the day of splitting. Images are projection of Z-stack. **C**, Distribution of gray value (higher value is whiter) and area of all organoids in same experiment as B. Percentages are relative to total number of organoids in that treatment. Plot shows distribution of in total 2,310 organoids, representative result of 5 mice. **D**, Time points for RNAseq experiment from small intestinal organoids treated with 10 ng/mL cytokine. **E**, PCA plot of log2(TPM + 1) values determined with RNAseq as shown in D. Each circle is one biological replicate. **F**, Number of up-regulated significant genes from same RNAseq experiment as in D ($p<0.05$ and log2fc>1). **G**, GSEA using genesets consisting of the 300 most significantly up-regulated genes from intestinal epithelium from mice infected with *N. brasiliensis* or *C. rodentium*. These genesets are compared to RNAseq of intestinal organoids stimulated with indicated cytokine compared to control. See supplementary file 1 for genesets. NES = normalised enrichment score.

IL-13 and IL-22 induce different gene signatures in goblet cells

To test the effect of IFNγ, IL-13 and IL-22 on cell lineage differentiation, we used cell-type specific gene signatures acquired through scRNAseq (*16*). GSEA revealed that these cytokines broadly

affect intestinal cell lineage differentiation in an expected manner (Fig. 2A). For example, giving IL-13 to organoids induced a tuft cell signature, supported by tuft cell staining *in vitro* (Fig. S2C) and *in vivo* upon *N. brasiliensis* infection (Fig. S4C,D,E). In addition, both IL-13 and IL-22 induced a goblet-cell associated gene signature (Fig. 2A). However, close examination showed that each cytokine induced a different set of goblet-cell genes with relatively little overlap both after 24 and 72 hours of cytokine stimulation (Fig. 2B, S5A), see supplementary file 2 for complete gene lists. This is exemplified by goblet cell markers *Muc2* and *Clca1* being specifically induced by IL-13 whereas another goblet cell marker, RELMβ (*Retnlb*), was induced more strongly by IL-22 (Fig. 2C, S5B). Even though not all mucins are goblet cell specific (*17*), we found mucin genes to have different expression patterns between IL-13 and IL-22 treatment (Fig. S5C). Confocal staining confirms that MUC2 was induced by IL-13 (Fig. 2D,F), and that RELMβ was more strongly induced by IL-22 (Fig. 2E,G). We noted that IL-22 induced (RELMβ+) goblet cells also looked different from those induced by IL-13 and often lacked large granule-like structures (Fig. 2E). To determine if these cells where positive for *Muc2* by mRNA, we combined staining of *Muc2* by RNAscope with MUC2 protein staining (Fig. S5D). We found that IL-22 led to the expansion of *Muc2*-high cells with patterns mimicking (RELMβ+) staining (Fig. S5D). These cells also had low MUC2 protein levels. Canonical differentiation of goblet cells occurs through inhibition of NOTCH and relies on transcription factors ATOH1 and SPDEF (*18*). Indeed, IL-13 induced *Atoh1* and *Spdef*, however, IL-22 did not, indicating that IL-22 induces goblet cell genes in a non-typical manner (Fig. 2H, S5E). It is not clear from these results what mechanism leads to induction of IL-22 dependent goblet cell, but RNAseq of early time points after IL-22 stimulation show that *Relmβ* is induced after just a few hours and GSEA of IL-22 specific goblet cell genes show significant enrichment after just 4 hours (Fig. S5F, 2I). These results indicate that IL-22 specific goblet cell genes are relative direct targets of IL-22. Furthermore, GO-term analysis of the goblet cell genes uniquely induced by IL-13 and IL-22 revealed different terms, for example, "response to endoplasmatic stress" was the top GO term associated with goblet cell genes induced by IL-22 (Fig. S5G,H). Taken together, we propose that cytokine-driven goblet cell responses are

linked to their function. IL-13 would primarily induce mucus to aid in parasite clearance whereas IL-22 responses are characterized by induction of antimicrobials to kill extracellular pathogens. More specifically, IL-13 leads to a quantitative increase in relative goblet cell numbers, whereas IL-22 treatment leads to a change in qualitative goblet cellular state including the induction of high levels of RELMβ.

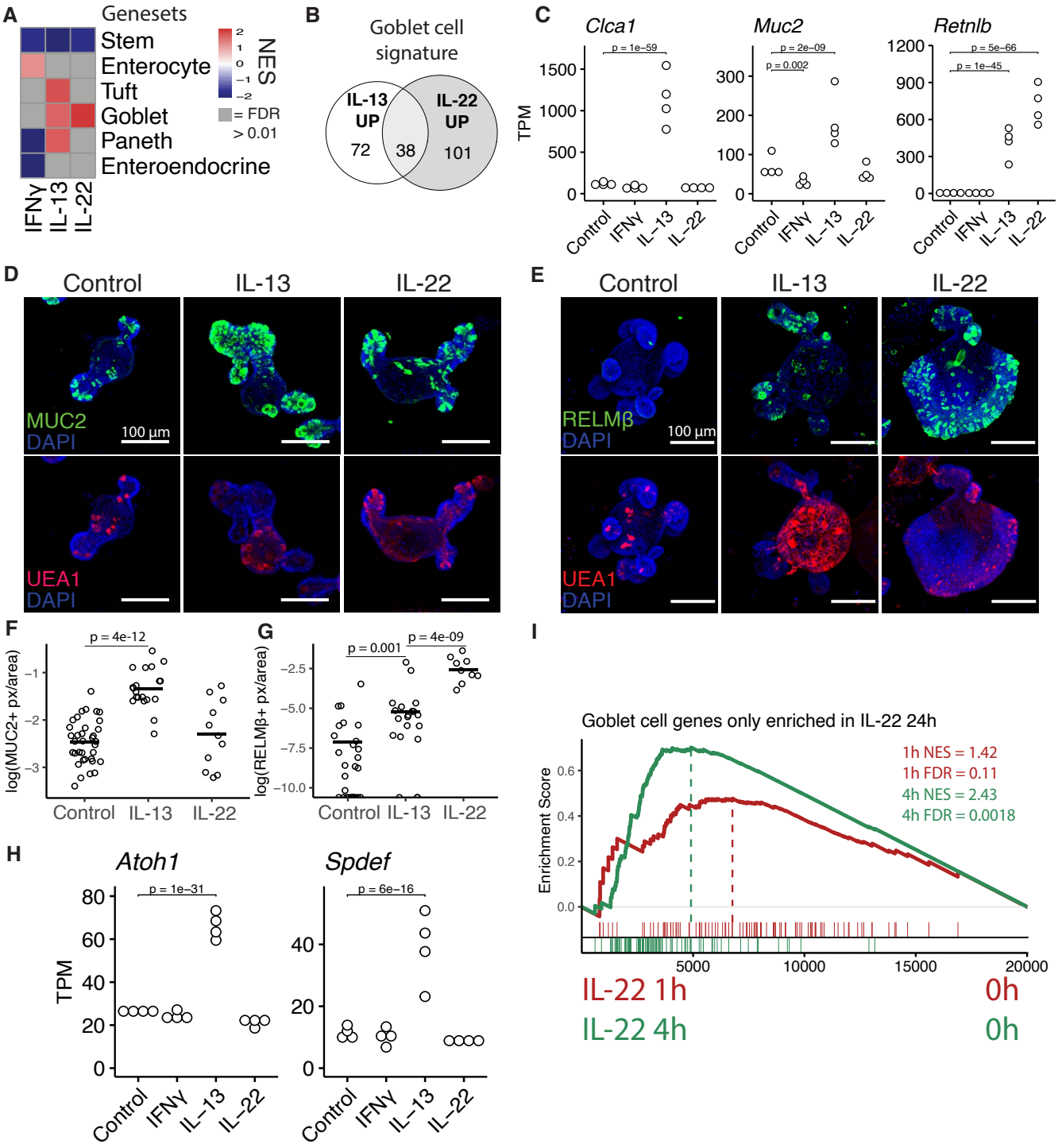

Figure 2: IL-13 and IL-22 induce different subsets of goblet cell genes. Caption continued on the next page.

Figure 2: (Continued caption.) **A**, Heatmap of NES values from GSEA analysis of gene sets representing different cell types compared to RNAseq data from organoids treated for 24 hours with cytokines, see supplementary file 1 for gene sets. **B**, Distribution of how the goblet cell gene set from plate based scRNAseq from Haber et al is changed upon 24 hour IL-13 and IL-22 treatment in organoids. Up is defined as log2fc>0.5 and p-adj<0.05. **C**, Gene expression from intestinal organoids treated for 24 hours with indicated cytokine. Statistics calculated with DESeq2, details in methods. **D**, **E**, Confocal staining of MUC2 and UEA1 2 days after splitting (D) and RELMβ and UEA1 at 3 days after splitting (E) in small intestinal organoids. Representative images of three mice. 5 ng/mL of IL-22 and 10 ng/mL of IL-13 was used. **F**,**G**, Quantification of images acquired as in D and E. Pixels are defined as positive above a set threshold. Each circle represents one organoid and statistics calculated with unpaired two tailed T-test. **H**, See C. **I**, GSEA of IL-22 specific goblet cell genes from B compared to RNAseq data from organoids stimulated with IL-22 for 1h and 4h. All images are projections of Z-stacks.

BMP signaling is associated with IL-13 and limits tuft cell differentiation *in vitro*

We were interested in how cytokines control mechanisms that define cell fate in the intestinal epithelium. Intestinal epithelium relies on NOTCH-, WNT-, BMP- and HIPPO-signaling to maintain homeostatic differentiation of cell lineages. We hypothesized that cytokines may use these developmental pathways in directing epithelial cell differentiation. We generated gene sets for these different pathways from published transcriptome datasets (*19*–*22*). GSEA analysis revealed that cytokines, and in particular IL-13 and IL-22, alter transcription of genes normally associated with HIPPO, NOTCH, and BMP pathways (Fig. 3A).

We were somewhat surprised to find a strong enrichment of BMP signaling upon IL-13 treatment. BMP members are traditionally expressed by mesenchymal cells, so it is unclear how IL-13 may induce BMP signaling. Nonetheless, established BMP target genes *Id1* and *Id3* (*20*), are upregulated specifically after IL-13 treatment (Fig. 3B). Next, we assessed the expression pattern of the TGF-β family members and surprisingly found that IL-13 robustly induced *Bmp2* and *Bmp8b* but not any other members (Fig. 3C, S6A). The change in the Bmp2 gene also was reflected with an increase of BMP2 protein secreted by organoids stimulated with IL-13 (Fig. 3D). In support, there was also an increase of *Bmp2* during a *N. brasiliensis* infection (Fig. 3E). Interestingly, Haber et al. lists *Bmp2* as a bona fide tuft cell marker in their gene sets from plate-based

scRNAseq of small intestinal epithelium (Fig. 3F) (*16*). The connection between tuft cells and IL-13 signaling is further highlighted by the fact that tuft cells specifically expressed high levels of *IL13ra1* as noted by Haber et al., whereas *IL4ra* or other cytokine receptors did not have such skewed cell-type specific receptor expression (Fig. S6B-D). In addition, tuft cells have increased pSTAT6 levels compared to other lineages (*23*). To test whether BMP signaling affects tuft cell differentiation, we compared organoids grown in normal EGF, NOGGIN, and RSPO (ENR) media with organoids grown without the presence of the BMP antagonist NOGGIN (ER media). Thus, taking away the obstructing factor for BMP activation. Organoids grown with NOGGIN in the media showed enrichment for a tuft cell signature and had higher expression of established tuft cell markers (Fig. 3G,H). Furthermore, antibody staining of the tuft cell marker DCLK1 revealed higher levels of tuft cells in organoids grown in the presence of NOGGIN (Fig. 3I,J).

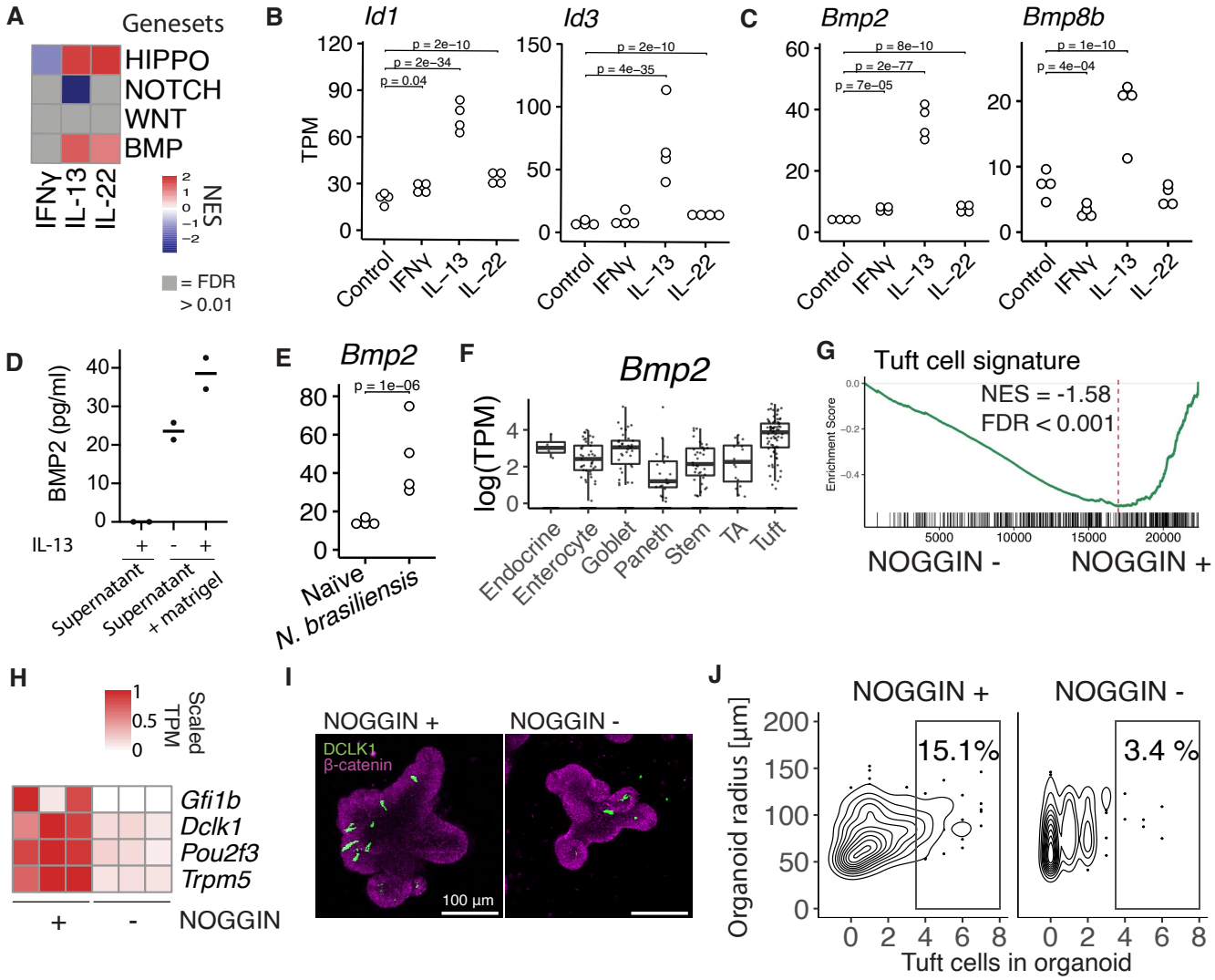

Figure 3: IL-13 induce BMP2 in intestinal epithelium. **A**, GSEA analysis of gene sets representing developmental pathways important in IEC development of bulk RNAseq data from organoids treated with 10 ng/mL cytokine for 24 hours. Gene set sources: HIPPO: Genes up in artifical YAP induction and down-regulated in YAP-KO. WNT: Genes up in organoids treated with the GSK3 inhibitor CHIR, NOTCH: Genes up in organoids from ATOH1 KO epithelium compared to wt and BMP: Genes up in organoid treated with BMP4 compared to control. Gene sets and references in supplementary file 1. **B**,**C**, Gene expression in small intestinal organoids treated with cytokines for 24 hours determined with RNAseq. Each dot is one biological replicate. **D**, Concentration of BMP2 in supernatant or supernatant+matrigel (without organoids) of organoids stimulated with IL-13 determined with ELISA. Each dot is one biological replicate. Representative of two experiments. **E**, Gene expression in epithelium from duodenum extracted from mice infected with *N. brasiliensis* determined with RNAseq. Each dot is one biological replicate. **F**, Plate based scRNAseq expression data from Haber et al in small intestinal epithelium. TA = Transit amplifying. **G**, GSEA of tuft cell gene set on RNAseq of small intestinal organoids grown in the presence of NOGGIN or not for 5 days since splitting. **H**, Tuft cell marker genes from same RNAseq data as G. **I**, DCLK1 confocal staining of small intestinal organoids grown in the presence of NOGGIN or not for 72 hours since splitting. Images are projections of Z-stacks. **J**, Quantitation of experiment in I. Representative of two experiments. Plot shows a total of 462 organoids. TPM = transcripts per million, NES = normalized enrichment score.

BMP signaling acts as a feedback loop to limit tuft cell expansion

Tuft cells are crucial mediators of parasitic immunity. In a feed-forward loop, tuft cells amplify ILC2s by expressing IL-25, and ILC2s, in turn, express IL-13 to expand tuft cells (*5*–*7*). Our findings so far may suggest a novel mechanism that IL-13 treatment induces an epithelial-intrinsic feedback loop mediated by BMP signaling. To further investigate this, we tested the ALK2 (BMP type I receptor) inhibitor dorsomorphin homolog 1 (DMH1) in combination with IL-13 (*24*) (Fig. 4A). We found that DMH1 completely blocked the induction of canonical BMP target genes *Id1* and *Id3* (Fig. 4B), but did not affect IL-13-induced *Bmp2* expression (Fig. 4C). Furthermore, the overall enrichment of BMP signaling target genes by IL-13 is blocked by DMH1, without modulating the effect of IL-13 on HIPPO or NOTCH target genes (Fig. 4D). Although DMH1 in itself did not change expression of tuft cell-associated genes such as *Dclk1*, *Pou2f3*, *Trpm5*, and *Alox5*, it did increase the expression of these genes when combined with IL-13 (Fig. 4E). The tuft cell marker gene *Il25* could not be detected in our RNAseq, but we did see an increase in *Il25* in IL-13+DMH1 treatmed compared to DMH1 alone when we tested this separately by qPCR (Fig. S7A). In support, the tuft cell gene signature was enriched in IL-13 + DMH1 compared to IL-13 by GSEA analysis while no other cell type gene signature was altered (Fig. 4F). Confocal staining confirmed the specific enrichment of tuft cells upon combination treatment of IL-13 and DMH1 (Fig. 4G,H,I). In addition, we noted that IL-13 also induced expression of the TGF-β induced gene *Tgfbi*, independently of ALK2 (Fig. 4J), and this also occurred after *N. brasiliensis* infection (Fig. 4K). BMP signaling is complex and is mediated by multiple receptors. For example, BMP2 can activate both SMAD1/5/8 (BMP) and SMAD2/3 (TGF-β) signaling (*25*). Therefore, we decided to also test SB525334, an inhibitor for the TGF-β type I receptor ALK5. Just as seen with DMH1, we see an increase in IL-13 induced tuft cells in organoids treated with SB525334 in a dose-dependent manner (Fig. 4L, S7B,C). Together, this supports a model in which activation of BMP and/or TGF-β signaling limits IL-13-induced tuft cell differentiation, thus, providing a feedback loop to limit tuft cell expansion during immune responses.

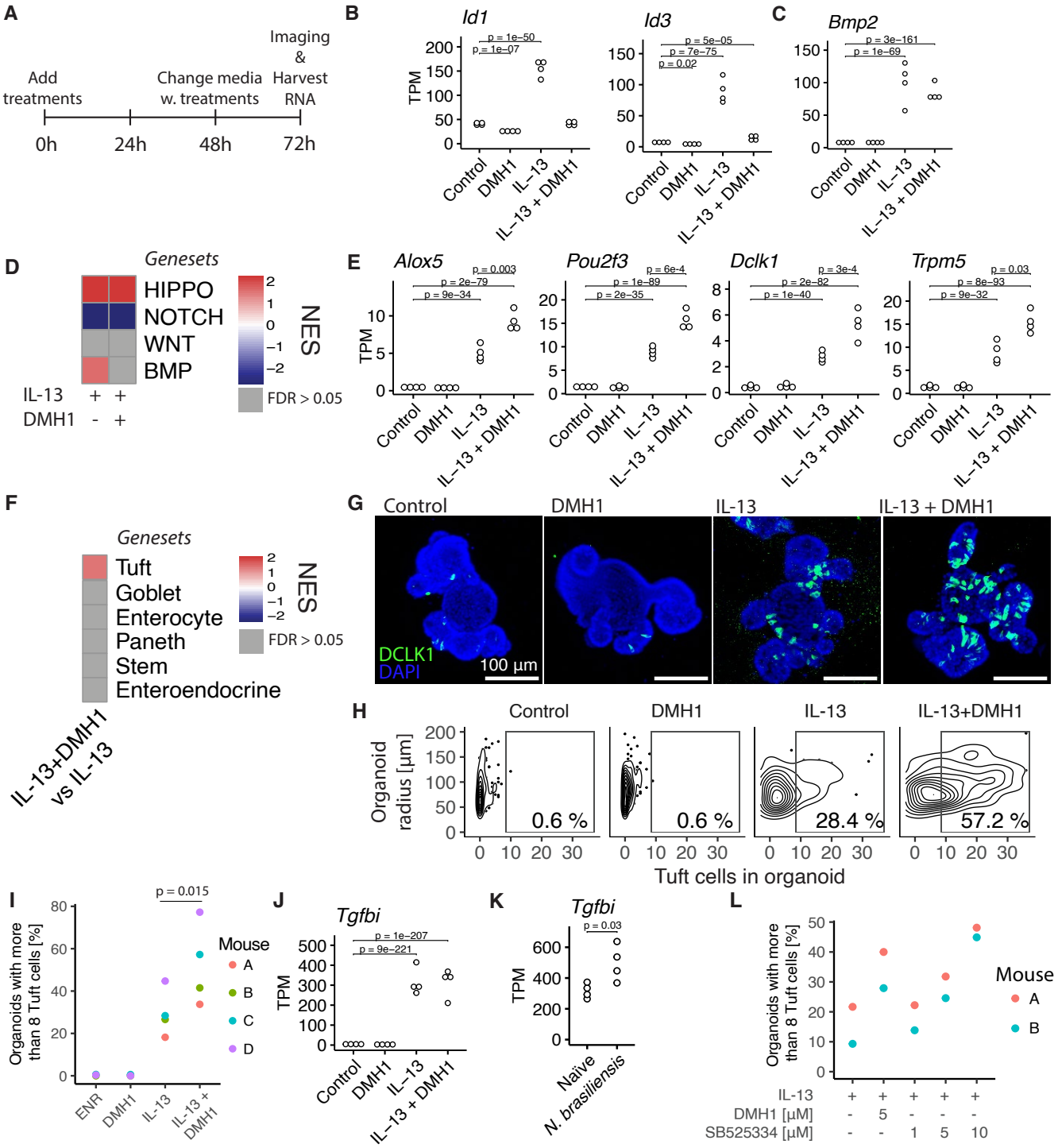

Figure 4: BMP signaling restricts IL-13-induced tuft cell expansion. Caption continued on next page.

Figure 4: (Continued caption.) **A**, Time points since seeding for RNAseq experiment from small intestinal organoids treated with 10 ng/mL cytokine and 5 µM DMH1 for 72 hours. **B**,**C**, Gene expression determined with RNAseq as described in A. Each circle is one biological replicate and statistics calculated with DESeq2, see methods. **D**, Heatmap of NES values from GSEA of gene sets representing signaling pathways in indicated treatments vs control condition. See supplementary file 1 for exact gene sets. **E**, see B. **F**, Heatmap of NES values from GSEA of gene sets representing cell types from Haber et al. in IL-13 + DMH1 treated organoids vs IL-13 organoids. See supplementary file 1 for exact gene sets. **G**, Confocal staining of DCLK1 in small intestinal organoids treated with indicated treatments for 72 hours. Images are projections of Z-stacks. **H**, Manual quantification of same experiment as G, plot represents a total of 566 organoids. **I**, Percentage determined as in H where each circle is a biological replicate from independent experiments. *p*-value determined with a paired T-test. **J**, See B. **K**, Gene expression in intestinal epithelium extracted from mice infected with *N. brasiliensis* determined with RNAseq. Each circle is one biological replicate and statistics calculated with DESeq2, see methods. **L**, Percentage of organoids with more than 8 tuft cells. Determined in similar fashion as in previous figures (see G,H and I) except that this is automatic tuft cell counts. Each circle is one biological replicate. Representative of two experiments. DMH1 inhibits ALK2 and SB525334 inhibits ALK5. TPM = transcripts per million, NES = Normalized Enrichment Score.

IL-13 activates BMP signaling in stem cells

To gain further insight into what role BMP signaling plays in the effect of IL-13 on the intestinal epithelium we stimulated small intestinal organoids with IL-13 for 1, 4, 8 and 24 hours with and without DMH1 (Fig. 5A). We found that IL-13 itself rapidly affects the transcriptome with 91 significantly changed genes after 1 hour compared to untreated, and 770 genes after 8 hours ($p<0.01$). In contrast, comparing DMH1+IL-13 *vs.* IL-13 we found a slower response with only 13 significantly changed genes after 8 hours, but 188 genes after 24 hours ($p<0.01$) (Fig. 5B). This suggests that BMP target genes are not early response genes upon IL-13 treatment. In accordance, we find that *Bmp2* and *Bmp8b* is rapidly induced after 1 hour (Fig. 5C, S8A), whereas maximal upregulation of canonical BMP target genes *Id1* and *Id3* and TGF-β target gene *Tgfbi* occurs only after 24 hours (Fig. 5D, S8B). Together, we propose that IL-13 mediated BMP signaling is mediated by rapid induction of BMP family members such as *Bmp2* and *Bmp8b* to subsequently activate BMP receptors.

We have found that BMP signaling limits IL-13-mediated tuft cell expansion (Fig. 4 and 5). To determine the cellular sequence of events, we downloaded and re-analyzed a scRNAseq data set

from small intestinal organoids that were treated with IL-13 (Fig. 5E) (*3*). We split the tuft cell population in two, and by RNA velocity analysis we found that there is a tuft progenitor (with closer proximity to the stem cell population) and a mature tuft cell population (Fig. 5F). The mature tuft cells have a high expression of *Dclk1*, *Pou2f3* is expressed in both populations, and *Sox4* is specific for tuft cell progenitors (Fig. 5G). The trancription factor *Sox4* has previously been found to be important in tuft cell development (*26*). Although *Sox4* has been associated with the intestinal stem cell signature (*27*), in this dataset it is more highly correlated with progenitor tuft cells (Fig. 5G). Qi et al. found that mice with an inducible epithelial specific knock out of *Bmpr1a* (ALK3) had up-regulation of *Sox4* expression in *Lgr5*+ stem cells and that *Sox4* is down-regulated in *Lgr5*+ stem cells from intestinal organoids stimulated with BMP4 (*20*), indicating that BMP signaling might actively regulate the amount of *Sox4* positive tuft cell progenitors. To investigate where BMP signaling affected tuft cell development we plotted *Id1* and *Id3* expression and found them to be specifically induced in stem cells by IL-13 (Fig. 5H). Furthermore, *Sox4* is rapidly induced by IL-13 before it returns to homeostasis levels after 24 hours and this down-regulation is not seen in 24 hours of IL-13 stimulation with DMH1 (Fig. 5I). This result is supported by our 72 hour stimulation data where we see an up-regulation of *Sox4* in IL-13 + DMH1 compared to IL-13 (Fig. 5J). We were not able to associate receptor (*Acvr1*) expression to stem cells specifically (Fig. S8C), so how stem-cell enriched responses occur is unclear. In summary, these data indicate a model where IL-13 induces differentiation of stem cells into tuft cell progenitors positive for *Sox4*. At the same time, IL-13 induces production of BMP signaling molecules, which act on stem cells and inhibits them from developing into *Sox4* positive tuft cell progenitors.

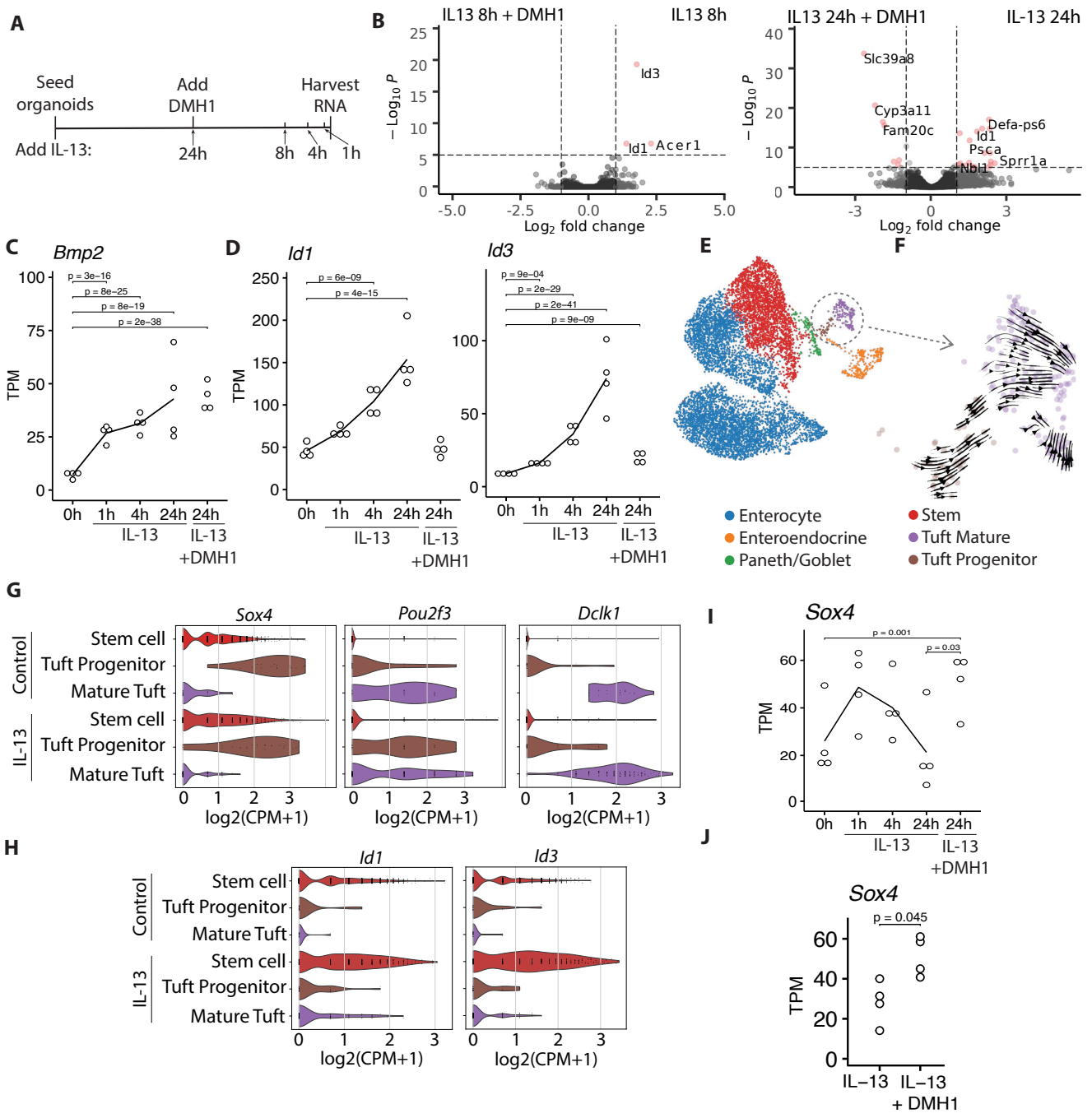

Figure 5: IL-13 activates BMP signaling in stem cells, skewing them away from tuft cell progenitors. **A**, Time points for RNAseq experiment from small intestinal organoids treated with 10 ng/mL cytokine at indicated timepoints and with and without 5 µM DMH1 for 24 hours. **B**, Volcano plots comparing indicated treatments from experiment described in A. **C**, **D**, Gene expression of experiment described in A. Each circle is one biological replicate, statistics calculated with DESeq2, see methods. **E**, scRNAseq data of small intestinal organoids treated with IL-13 and untreated from Biton et al (*3*). **F**, RNA velocity analysis of tuft cell populations from scRNAseq data presented in E. **G**, **H**, Violin plots of gene expression in tuft cells from scRNAseq data presented in E. **I**, See C. **J**, Gene expression of small intestinal organoids treated with indicated treatment for 72 hours. Each circle is one biological replicate, statistics calculated with DESeq2, see methods. TPM = transcripts per million, CPM = Counts per million.

BMP signaling restricts *N. brasiliensis* induced tuft cell expansion *in vivo*

Organoid work allows us to study intestinal epithelial mechanisms in isolation. However, *in vivo* there are many additional cell types that together orchestrate immunity to infection. To investigate the role of ALK2 signaling in *N. brasiliensis*-induced tuft cell hyperplasia, we injected mice with either DMH1 or its solvent (DMSO) intraperitoneally every other day starting one day before infection (Fig. 6A). Confocal staining of DCLK1 revealed an increase in the number of tuft cells at both day 6 and day 8 after infection when comparing DMH1-treated to DMSO-treated animals (Fig. 6B,C). The increase in tuft cells was also associated with a non-significant increase in *Il25* but not *Il13* (Fig. S9A). No difference was found in RELMβ or UEA1 (goblet) positive cells, indicating that the difference is specific to tuft cells (Fig. 6D-F).

To test if BMP/TGF-β signalling is altered during infection we performed pSMAD2 staining (Fig. 7A,B). We found that there was a significant induction of nuclear pSMAD2 levels in crypt cells of infected mice compared to uninfected mice, and that this induction required ALK2 signalling as it did not occur in DMH1-treated mice (Fig. 7A,B). Based on our organoid work, we proposed that BMP/TGF-β signalling leads to repression of *Sox4* (Fig. 5G,I,J). Indeed we find a reduction of crypt-base located *Sox4* levels after infection and this repression did not occur in DMH1-treated animals (Fig. 7C,D). As reported by others, we found *Sox4* enriched at the stem cell zone (*26*, *27*), however, the reduction of *Sox4* did not lead to a reduction of numbers of intestinal stem cells, as measured by counting OLFM4+ cells in crypts (Fig. 7E,F). Nor did it affect crypt proliferation as assessed by Ki67 staining (Fig. S9B,C) or apoptosis as assessed with cleaved Caspase3 staining (Fig. S9D,E). Finally, we investigated the association between *Bmp2* and tuft cells *in vivo* by using RNAscope probes for *Bmp2* and *Dclk1* we found *Bmp2* to be associated with tuft cells in the crypt (Fig. 7G,H). This association is not exclusive to tuft cells as we do see *Bmp2* in non-tuft cells, especially in the villus tip, a conclusion which is supported by the association of *Bmp2* with both enterocytes and tuft cells in organoids stimulated with IL-13 from scRNAseq data from (*3*) (Fig 7I). Taken together, these results suggest that BMP/TGF-β signaling restricts *N. brasiliensis*

dependent tuft cell expansion *in vivo* by controlling *Sox4* expression.

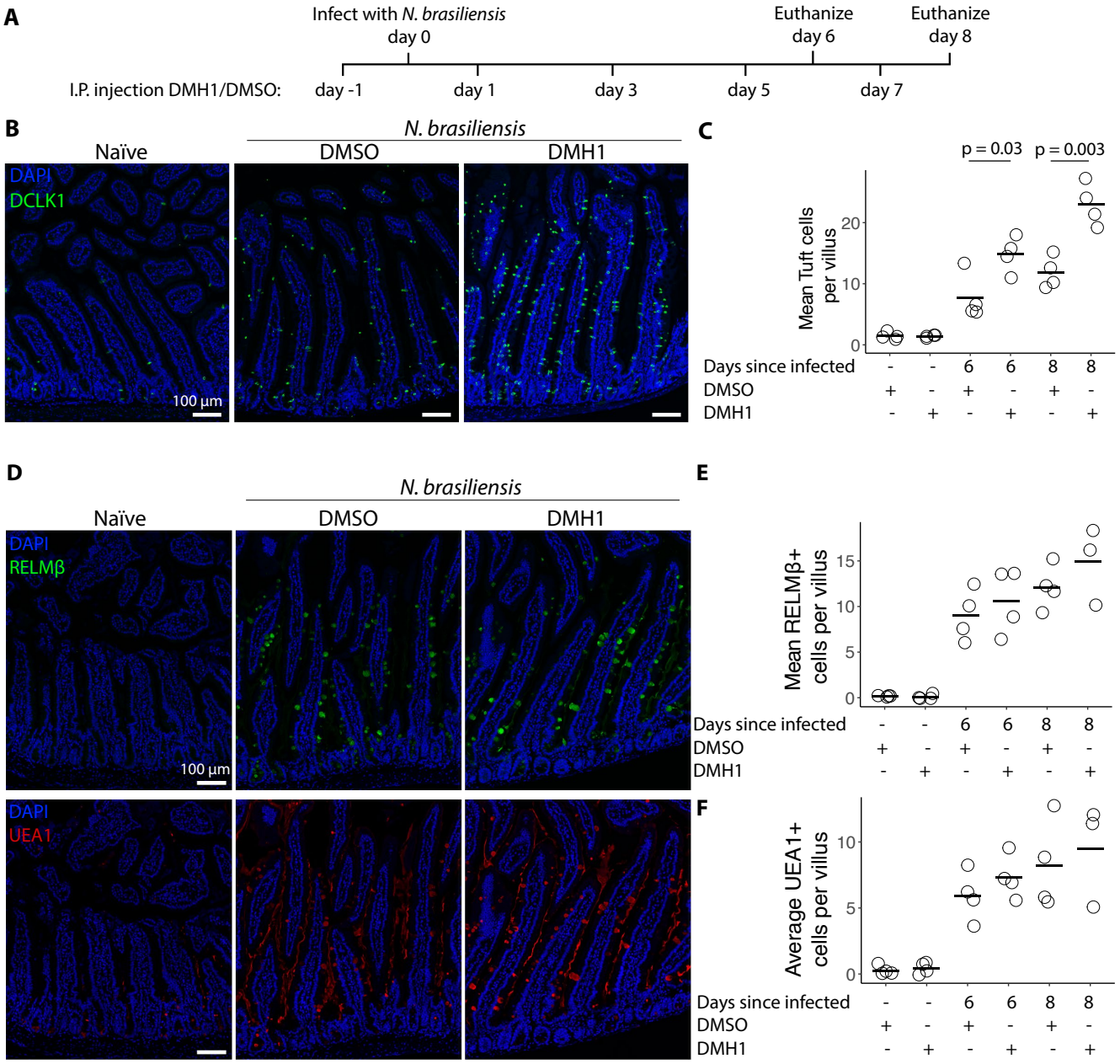

Figure 6: BMP signaling restricts *N. brasiliensis* induced tuft cell expansion *in vivo*. **A**, Timeline of *N. brasiliensis* infection and intraperitoneal injection of 5 µM DMH1 dissolved in DMSO or solvent alone. **B**, DCLK1 antibody staining of duodenum from mice 8 days after infection with *N. brasiliensis* and injected with DMH1 according to timeline shown in A. **C**, Quantification of images shown in B and additional images. Each dot represents one mouse. Statistics calculated with unpaired two tailed T-test. **D**, RELMβ antibody and UEA1 staining of duodenum from mice 8 days after infection with *N. brasiliensis* and injected with DMH1 according to timeline shown in A. **E**, **F**, Quantification of images shown in D and additonal images. Each dot represents one mouse.

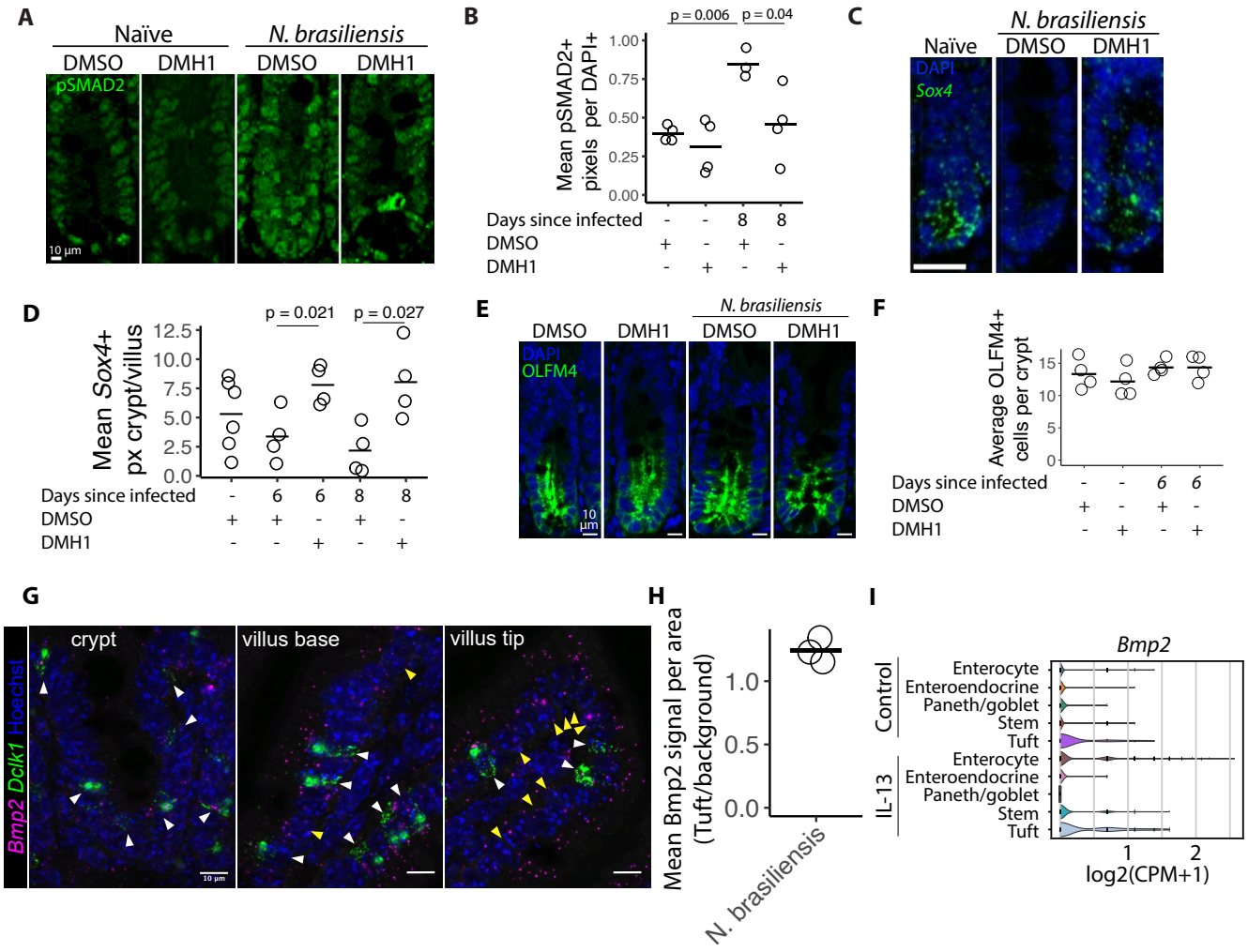

Figure 7: DMH1 restricts *N.brasiliensis* induced BMP signalling. **A**, pSMAD2 antibody staining in crypts from duodenum from mice 8 days after infection with *N. brasiliensis*. DMSO or DMH1 was injected every other day starting one day before infection. **B**, Quantification of images shown in A. Each circle represents the mean of at least 5 crypts in one mouse measuring pSMAD2+ pixels divided by DAPI+ pixels. Statistics calculated with unpaired two tailed T-test. **C**, RNAscope probe for *Sox4* in in crypts from duodenum 8 days after infection. Scale bar is 25 µm. **D**, Quantification of images shown in C and additional images. Each circle represents the mean of at least 5 crypts in one mouse measuring *Sox4*+ pixels in the crypt divided by *Sox4*+ pixels in the villus. Statistics calculated with unpaired two tailed T-test. **E**, Confocal images of OLFM4 staining in in crypts from duodenum 6 days after infection. **F**, Quantification of images shown in E. Each dot represents the average of at least 5 crypts from one mouse. **G**, RNAscope probe for *Bmp2* in indicated tissue from duodenum 6 days after infection. **H**, Quantification of crypts from images shown in G. *Bmp2* signal per area was measured in the immediate vicinity of *Dclk1* signal divided by cells not positive for *Dclk1* (defined as background). Both tuft cell area and background area was manually defined and each circle represents one mouse. **I**, Violin plots of gene expression from scRNAseq data of small intestinal organoids treated with IL-13 and untreated from Biton et al (*3*).

Discussion

The intestinal epithelium is capable of rapidly altering its cellular composition to defend against pathogens. Here, we provide a comprehensive comparison of how different immune responses mechanistically drive changes in the intestinal epithelium. Specifically, we find that key cytokines associated with different modes of immunity influence developmental pathways to guide changes in epithelial composition.

In recent years, tuft cells have been identified as regulators of intestinal health in general (*9*), and have taken center stage in the defense against helminth infections specifically (*28*). They express receptors that help them detect helminths, which together with type 2 cytokines results in their expansion (*29*, *30*). This culminates in a feed forward loop where tuft cell derived IL-25 activates ILC2s and ILC2 derived IL-13 induces tuft cell differentiation (*5*–*7*). There are limits to this feed-forward loop though. For example, a putative epithelial-intrinsic PGD_2-CRTH2 axis counteracts the IL-13-induced epithelial response (*31*), and ILC2-expressed CISH blocks ILC2 activation, which in turn limits tuft cell expansion (*32*). Other, competing, cytokines can also affect this loop as IL-22 inhibits IL-13 induced tuft cell responses (*33*). Finally, pathogens may also take part. Two studies recently showed that *Heligmosomoides polygyrus* secreted products can inhibit tuft cell expansion, likely by reprogramming epithelium towards a fetal-like state (*34*, *35*).

Here, we identify that intestinal-epithelial intrinsic *Bmp* signaling can act as a brake on IL-13-induced tuft cell expansion (Fig. 4). We attribute this feedback mechanism to BMP/TGF-β signaling in general rather than a single BMP protein as we found both *Bmp2* and *Bmp8b* to be induced by IL-13 in organoids. In further support, the ALK5 inhibitor SB525334 show a similar ability as the ALK2 inhibitor DMH1 to increase tuft cell numbers upon IL-13 treatment. Our data indicate that the IL-13-mediated tuft cell hyperplasia is limited by BMP/TGF-β-dependent inhibition of *Sox4*. *Sox4*+ tuft cell progenitors are thus initially expanded by IL-13, and then repressed by BMP signalling. It is paradoxical that inhibition of BMP signaling can affect intestinal epithelial stem cells since the crypt is surrounded by BMP antagonists (*36*). However, these BMP

antagonists incompletely block BMP signaling as some pSMAD1/5/8 activation is still found in LGR5+ stem cells (*20*), and we observed a distinct increase of pSMAD2 in intestinal crypts upon infection with *N. brasiliensis* (Fig. 7). Furthermore, our experiments comparing IL-13 and IL-13+DMH1 are done in the presence of NOGGIN, a BMP inhibitor, indicating these crypt inhibitors only partly inhibit BMP signaling.

In addition to our findings regarding cytokine-driven tuft cell expansion, we also provide data suggesting that both IL-13 and IL-22 induce goblet cell gene signatures, but that these are different (Fig. 2). There have been conflicting reports in whether IL-22 influence goblet cell levels in intestinal epithelium. Some studies find that the number of MUC2+ cells are unchanged or reduced upon IL-22 treatment (*37*, *38*), however, a study that over express the IL-22 inhibitor IL-22BP in the gut found a reduction in goblet cells (*39*) and IL-22 knock out mice infected with *N. brasiliensis* have reduction in goblet cell induction as measured by Periodic acid schiff (PAS) staining (*40*). Additionally, the goblet-cell effector RELMβ is critical for resistance against both bacterial and helminth infections (*41*–*43*). We hypothesize that the difference between IL-13 and IL-22 induced goblet cells is related to the type of immune response. Immunity to parasites requires a 'weep and sweep' response, in which goblet cells play an essential role by secreting mucus (weeping) to facilitate the expulsion of helminths (*44*), whereas other responses may rely less on the induction of mucus and expansion of goblet cell numbers. Instead, we find that IL-22 rapidly induces goblet-cell specific ER stress response genes, which corroborates recent work that identified a pathologically relevant role for IL-22 (*45*).

Overall, our approach of stimulating intestinal organoids with cytokines has revealed that developmental pathways underlie the cellular compositional changes that occur as part of immune responses taking place in the intestine. In support, a recent study showed that Il17ra signalling in intestinal stem cells induces ATOH1, thereby inducing secretory cells through NOTCH signalling (*46*). These changes have been confirmed using relevant *in vivo* models of infection or inflammation. It is important to balance both active immunity/inflammation with resolution of inflammation, and many immunopathologies reflect the importance of maintaining this balance.

The discovery of an innate BMP-driven brake on IL-13 induced immune changes suggest that targeting this pathway may therefore be a useful tool to aid resolution of inflammation in clinically relevant diseases.

Acknowledgments

We thank the animal care (CoMed) and imaging (CMIC) core facilities that assisted in this work (NTNU). Part of the RNA-seq was done by the Genomics Core Facility at NTNU, which receives funding from the Faculty of Medicine and Health Sciences and Central Norway Regional Health Authority. This work was financially supported by the Norwegian Research Council (Centre of Excellence grant 223255/F50, and 'Young Research Talent' 274760 to MJO) and the Norwegian Cancer Society (182767 to MJO). This work was supported by the Wellcome Trust through Investigator Awards to RMM (Ref 106122 and 219530), and the Wellcome Trust core-funded Wellcome Centre for Integrative Parasitology (Ref 104111).

The authors have no conflicting financial interests.

Code and data availability

Code for brightfield and confocal analysis: `https://github.com/havardtl/coco`

Sequencing data is deposited in the ArrayExpress database (`http://www.ebi.ac.uk/arrayexpress`) under the following accession numbers:

- RNAseq of small intestinal organoids treated with cytokines for 24 hours: E-MTAB-9182
- RNAseq of duodenal intestinal epithelium from mice infected with *N. brasiliensis*: E-MTAB-9183
- RNAseq of colon intestinal epithelium from mice infected with *C. rodentium*: E-MTAB-9184

- RNAseq of small intestinal organoids treated for 72 hours with IL-13, IL-22 and DMH1: E-MTAB-9185
- RNAseq of small intestinal organoids treated with IL-13 for 0h, 1h, 4h, 8h and 24h with and without DMH1: E-MTAB-10455
- RNAseq of small intestinal organoids treated with IL-22 for 0h, 1h and 4h: E-MTAB-11273

References

1. M. D. Kirk, S. M. Pires, R. E. Black, M. Caipo, J. A. Crump, B. Devleesschauwer, D. Döpfer, A. Fazil, C. L. Fischer-Walker, T. Hald, A. J. Hall, K. H. Keddy, R. J. Lake, C. F. Lanata, P. R. Torgerson, A. H. Havelaar, F. J. Angulo, en, *PLOS Medicine* **12**, Publisher: Public Library of Science, e1001921, ISSN: 1549-1676 (Dec. 2015).
2. H. Spits, D. Artis, M. Colonna, A. Diefenbach, J. P. Di Santo, G. Eberl, S. Koyasu, R. M. Locksley, A. N. J. McKenzie, R. E. Mebius, F. Powrie, E. Vivier, en, *Nature Reviews Immunology* **13**, Number: 2 Publisher: Nature Publishing Group, 145–149, ISSN: 1474-1741 (Feb. 2013).
3. M. Biton, A. L. Haber, N. Rogel, G. Burgin, S. Beyaz, A. Schnell, O. Ashenberg, C.-W. Su, C. Smillie, K. Shekhar, Z. Chen, C. Wu, J. Ordovas-Montanes, D. Alvarez, R. H. Herbst, M. Zhang, I. Tirosh, D. Dionne, L. T. Nguyen, M. E. Xifaras, A. K. Shalek, U. H. von Andrian, D. B. Graham, O. Rozenblatt-Rosen, H. N. Shi, V. Kuchroo, O. H. Yilmaz, A. Regev, R. J. Xavier, en, *Cell* **175**, 1307–1320.e22, ISSN: 00928674 (Nov. 2018).
4. P. W. Tetteh, H. F. Farin, H. Clevers, en, *Trends in Cell Biology* **25**, 100–108, ISSN: 09628924 (Feb. 2015).
5. M. R. Howitt, S. Lavoie, M. Michaud, A. M. Blum, S. V. Tran, J. V. Weinstock, C. A. Gallini, K. Redding, R. F. Margolskee, L. C. Osborne, D. Artis, W. S. Garrett, en, *Science* **351**, 1329–1333, ISSN: 0036-8075, 1095-9203 (Mar. 2016).

6. F. Gerbe, E. Sidot, D. J. Smyth, M. Ohmoto, I. Matsumoto, V. Dardalhon, P. Cesses, L. Garnier, M. Pouzolles, B. Brulin, M. Bruschi, Y. Harcus, V. S. Zimmermann, N. Taylor, R. M. Maizels, P. Jay, en, *Nature* **529**, Number: 7585 Publisher: Nature Publishing Group, 226–230, ISSN: 1476-4687 (Jan. 2016).

7. J. von Moltke, M. Ji, H.-E. Liang, R. M. Locksley, en, *Nature* **529**, Number: 7585 Publisher: Nature Publishing Group, 221–225, ISSN: 1476-4687 (Jan. 2016).

8. A. Banerjee, C. A. Herring, B. Chen, H. Kim, A. J. Simmons, A. N. Southard-Smith, M. M. Allaman, J. R. White, M. C. Macedonia, E. T. Mckinley, M. A. Ramirez-Solano, E. A. Scoville, Q. Liu, K. T. Wilson, R. J. Coffey, M. K. Washington, J. A. Goettel, K. S. Lau, English, *Gastroenterology* **159**, Publisher: Elsevier, 2101–2115.e5, ISSN: 0016-5085, 1528-0012 (Dec. 2020).

9. S. K. Hendel, L. Kellermann, A. Hausmann, N. Bindslev, K. B. Jensen, O. H. Nielsen, *Frontiers in Immunology* **13**, ISSN: 1664-3224 (2022).

10. P. H. Dedhia, N. Bertaux-Skeirik, Y. Zavros, J. R. Spence, English, *Gastroenterology* **150**, Publisher: Elsevier, 1098–1112, ISSN: 0016-5085, 1528-0012 (May 2016).

11. D. Serra, U. Mayr, A. Boni, I. Lukonin, M. Rempfler, L. C. Meylan, M. B. Stadler, P. Strnad, P. Papasaikas, D. Vischi, A. Waldt, G. Roma, P. Liberali, En, *Nature*, 1, ISSN: 1476-4687 (Apr. 2019).

12. J. Ostrop, R. T. Zwiggelaar, M. Terndrup Pedersen, F. Gerbe, K. Bösl, H. T. Lindholm, A. Díez-Sánchez, N. Parmar, S. Radetzki, J. P. von Kries, P. Jay, K. B. Jensen, C. Arrowsmith, M. J. Oudhoff, English, *Frontiers in Cell and Developmental Biology* **8**, Publisher: Frontiers, ISSN: 2296-634X (2021).

13. C. A. Lindemans, M. Calafiore, A. M. Mertelsmann, M. H. O'Connor, J. A. Dudakov, R. R. Jenq, E. Velardi, L. F. Young, O. M. Smith, G. Lawrence, J. A. Ivanov, Y.-Y. Fu, S. Takashima, G. Hua, M. L. Martin, K. P. O'Rourke, Y.-H. Lo, M. Mokry, M. Romera-

Hernandez, T. Cupedo, L. E. Dow, E. E. Nieuwenhuis, N. F. Shroyer, C. Liu, R. Kolesnick, M. R. M. v. d. Brink, A. M. Hanash, en, *Nature* **528**, 560–564, ISSN: 1476-4687 (Dec. 2015).

14. H. F. Farin, W. R. Karthaus, P. Kujala, M. Rakhshandehroo, G. Schwank, R. G. J. Vries, E. Kalkhoven, E. E. S. Nieuwenhuis, H. Clevers, en, *Journal of Experimental Medicine* **211**, 1393–1405, ISSN: 0022-1007, 1540-9538 (June 2014).

15. F. Gerbe, J. H. van Es, L. Makrini, B. Brulin, G. Mellitzer, S. Robine, B. Romagnolo, N. F. Shroyer, J.-F. Bourgaux, C. Pignodel, H. Clevers, P. Jay, *Journal of Cell Biology* **192**, 767–780, ISSN: 0021-9525 (Mar. 2011).

16. A. L. Haber, M. Biton, N. Rogel, R. H. Herbst, K. Shekhar, C. Smillie, G. Burgin, T. M. Delorey, M. R. Howitt, Y. Katz, I. Tirosh, S. Beyaz, D. Dionne, M. Zhang, R. Raychowdhury, W. S. Garrett, O. Rozenblatt-Rosen, H. N. Shi, O. Yilmaz, R. J. Xavier, A. Regev, en, *Nature* **551**, 333–339, ISSN: 0028-0836, 1476-4687 (Nov. 2017).

17. T. Pelaseyed, J. H. Bergström, J. K. Gustafsson, A. Ermund, G. M. H. Birchenough, A. Schütte, S. van der Post, F. Svensson, A. M. Rodríguez-Piñeiro, E. E. Nyström, C. Wising, M. E. Johansson, G. C. Hansson, *Immunological reviews* **260**, 8–20, ISSN: 0105-2896 (July 2014).

18. T. K. Noah, A. Kazanjian, J. Whitsett, N. F. Shroyer, en, *Experimental Cell Research* **316**, 452–465, ISSN: 0014-4827 (Feb. 2010).

19. A. Gregorieff, Y. Liu, M. R. Inanlou, Y. Khomchuk, J. L. Wrana, en, *Nature* **526**, 715–718, ISSN: 0028-0836, 1476-4687 (Oct. 2015).

20. Z. Qi, Y. Li, B. Zhao, C. Xu, Y. Liu, H. Li, B. Zhang, X. Wang, X. Yang, W. Xie, B. Li, J.-D. J. Han, Y.-G. Chen, *Nature Communications* **8**, ISSN: 2041-1723 (Jan. 2017).

21. X. Yin, H. F. Farin, J. H. van Es, H. Clevers, R. Langer, J. M. Karp, en, *Nature Methods* **11**, 106–112, ISSN: 1548-7091, 1548-7105 (Jan. 2014).

22. T.-H. Kim, F. Li, I. Ferreiro-Neira, L.-L. Ho, A. Luyten, K. Nalapareddy, H. Long, M. Verzi, R. A. Shivdasani, en, *Nature* **506**, 511–515, ISSN: 0028-0836, 1476-4687 (Feb. 2014).

23. C. A. Herring, A. Banerjee, E. T. McKinley, A. J. Simmons, J. Ping, J. T. Roland, J. L. Franklin, Q. Liu, M. J. Gerdes, R. J. Coffey, K. S. Lau, en, *Cell Systems* **6**, 37–51.e9, ISSN: 2405-4712 (Jan. 2018).

24. A. H. Mohedas, X. Xing, K. A. Armstrong, A. N. Bullock, G. D. Cuny, P. B. Yu, *ACS Chemical Biology* **8**, Publisher: American Chemical Society, 1291–1302, ISSN: 1554-8929 (June 2013).

25. A. Holtzhausen, C. Golzio, T. How, Y.-H. Lee, W. P. Schiemann, N. Katsanis, G. C. Blobe, en, *The FASEB Journal* **28**, _eprint: https://faseb.onlinelibrary.wiley.com/doi/pdf/10.1096/fj.13-239178, 1248–1267, ISSN: 1530-6860 (2014).

26. A. D. Gracz, L. A. Samsa, M. J. Fordham, D. C. Trotier, B. Zwarycz, Y.-H. Lo, K. Bao, J. Starmer, J. R. Raab, N. F. Shroyer, R. L. Reinhardt, S. T. Magness, en, *Gastroenterology* **155**, 1508–1523.e10, ISSN: 0016-5085 (Nov. 2018).

27. J. Muñoz, D. E. Stange, A. G. Schepers, M. v. d. Wetering, B.-K. Koo, S. Itzkovitz, R. Volckmann, K. S. Kung, J. Koster, S. Radulescu, K. Myant, R. Versteeg, O. J. Sansom, J. H. v. Es, N. Barker, A. v. Oudenaarden, S. Mohammed, A. J. R. Heck, H. Clevers, en, *The EMBO Journal* **31**, 3079–3091, ISSN: 0261-4189, 1460-2075 (July 2012).

28. C. Schneider, C. E. O'Leary, R. M. Locksley, en, *Nature Reviews Immunology* **19**, 584–593, ISSN: 1474-1741 (Sept. 2019).

29. C. Schneider, C. E. O'Leary, J. von Moltke, H.-E. Liang, Q. Y. Ang, P. J. Turnbaugh, S. Radhakrishnan, M. Pellizzon, A. Ma, R. M. Locksley, English, *Cell* **174**, 271–284.e14, ISSN: 0092-8674, 1097-4172 (July 2018).

30. M. S. Nadjsombati, J. W. McGinty, M. R. Lyons-Cohen, J. B. Jaffe, L. DiPeso, C. Schneider, C. N. Miller, J. L. Pollack, G. Nagana Gowda, M. F. Fontana, D. J. Erle, M. S. Anderson, R. M. Locksley, D. Raftery, J. von Moltke, en, *Immunity* **49**, 33–41.e7, ISSN: 10747613 (July 2018).

31. O. O. Oyesola, M. T. Shanahan, M. Kanke, B. M. Mooney, L. M. Webb, S. Smita, M. K. Matheson, P. Campioli, D. Pham, S. P. Früh, J. W. McGinty, M. J. Churchill, J. L. Cahoon, P. Sundaravaradan, B. A. Flitter, K. Mouli, M. S. Nadjsombati, E. Kamynina, S. A. Peng, R. L. Cubitt, K. Gronert, J. D. Lord, I. Rauch, J. von Moltke, P. Sethupathy, E. D. Tait Wojno, *Journal of Experimental Medicine* **218**, e20202178, ISSN: 0022-1007 (July 2021).

32. M. E. Kotas, N. M. Mroz, S. Koga, H.-E. Liang, A. W. Schroeder, R. R. Ricardo-Gonzalez, C. Schneider, R. M. Locksley, en, *Mucosal Immunology* **14**, Number: 6 Publisher: Nature Publishing Group, 1295–1305, ISSN: 1935-3456 (Nov. 2021).

33. Z. Fu, J. W. Dean, L. Xiong, M. W. Dougherty, K. N. Oliff, Z.-m. E. Chen, C. Jobin, T. J. Garrett, L. Zhou, en, *Nature Communications* **12**, Number: 1 Publisher: Nature Publishing Group, 4462, ISSN: 2041-1723 (July 2021).

34. C. Drurey, H. T. Lindholm, G. Coakley, M. C. Poveda, S. Löser, R. Doolan, F. Gerbe, P. Jay, N. Harris, M. J. Oudhoff, R. M. Maizels, *Journal of Experimental Medicine* **219**, e20211140, ISSN: 0022-1007 (Nov. 2021).

35. D. Karo-Atar, S. Ouladan, T. Javkar, L. Joumier, M. K. Matheson, S. Merritt, S. Westfall, A. Rochette, M. E. Gentile, G. Fontes, G. J. Fonseca, M. Parisien, L. Diatchenko, J. v. Moltke, M. Malleshaiah, A. Gregorieff, I. L. King, "Direct reprogramming of the intestinal epithelium by parasitic helminths subverts type 2 immunity", en, tech. rep., Section: New Results Type: article (bioRxiv, Sept. 2021), p. 2021.09.25.461778.

36. C. Kosinski, V. S. W. Li, A. S. Y. Chan, J. Zhang, C. Ho, W. Y. Tsui, T. L. Chan, R. C. Mifflin, D. W. Powell, S. T. Yuen, S. Y. Leung, X. Chen, en, *Proceedings of the National Academy of Sciences* **104**, Publisher: National Academy of Sciences Section: Biological Sciences, 15418–15423, ISSN: 0027-8424, 1091-6490 (Sept. 2007).

37. X. Zhang, S. Liu, Y. Wang, H. Hu, L. Li, Y. Wu, D. Cao, Y. Cai, J. Zhang, X. Zhang, *International Journal of Molecular Medicine* **43**, Publisher: Spandidos Publications, 1657–1668, ISSN: 1107-3756 (Apr. 2019).

38. J.-M. Zha, H.-S. Li, Q. Lin, W.-T. Kuo, Z.-H. Jiang, P.-Y. Tsai, N. Ding, J. Wu, S.-F. Xu, Y.-T. Wang, J. Pan, X.-M. Zhou, K. Chen, M. Tao, M. A. Odenwald, A. Tamura, S. Tsukita, J. R. Turner, W.-Q. He, *Cellular and Molecular Gastroenterology and Hepatology* **7**, 255–274, ISSN: 2352-345X (Jan. 2019).

39. K. Sugimoto, A. Ogawa, E. Mizoguchi, Y. Shimomura, A. Andoh, A. K. Bhan, R. S. Blumberg, R. J. Xavier, A. Mizoguchi, en, *Journal of Clinical Investigation*, JCI33194, ISSN: 0021-9738 (Jan. 2008).

40. J.-E. Turner, B. Stockinger, H. Helmby, en, *PLOS Pathogens* **9**, Publisher: Public Library of Science, e1003698, ISSN: 1553-7374 (Oct. 2013).

41. D. Artis, M. L. Wang, S. A. Keilbaugh, W. He, M. Brenes, G. P. Swain, P. A. Knight, D. D. Donaldson, M. A. Lazar, H. R. P. Miller, G. A. Schad, P. Scott, G. D. Wu, en, *Proceedings of the National Academy of Sciences* **101**, ISBN: 9780404034108 Publisher: National Academy of Sciences Section: Biological Sciences, 13596–13600, ISSN: 0027-8424, 1091-6490 (Sept. 2004).

42. D. C. Propheter, A. L. Chara, T. A. Harris, K. A. Ruhn, L. V. Hooper, en, *Proceedings of the National Academy of Sciences* **114**, 11027–11033, ISSN: 0027-8424, 1091-6490 (Oct. 2017).

43. K. S. B. Bergstrom, V. Morampudi, J. M. Chan, G. Bhinder, J. Lau, H. Yang, C. Ma, T. Huang, N. Ryz, H. P. Sham, M. Zarepour, C. Zaph, D. Artis, M. Nair, B. A. Vallance, en, *PLOS Pathogens* **11**, ed. by A. J. Baumler, e1005108, ISSN: 1553-7374 (Aug. 2015).

44. W. C. Gause, C. Rothlin, P. Loke, en, *Nature Reviews Immunology*, Publisher: Nature Publishing Group, 1–12, ISSN: 1474-1741 (May 2020).

45. N. Powell, E. Pantazi, P. Pavlidis, A. Tsakmaki, K. Li, F. Yang, A. Parker, C. Pin, D. Cozzetto, D. Minns, E. Stolarczyk, S. Saveljeva, R. Mohamed, P. Lavender, B. Afzali, J. Digby-Bell, T. Tjir-Li, A. Kaser, J. Friedman, T. T. MacDonald, G. A. Bewick, G. M. Lord, en, *Gut* **69**, Publisher: BMJ Publishing Group Section: Recent advances in basic science, 578–590, ISSN: 0017-5749, 1468-3288 (Mar. 2020).

46. X. Lin, S. J. Gaudino, K. K. Jang, T. Bahadur, A. Singh, A. Banerjee, M. Beaupre, T. Chu, H. T. Wong, C.-K. Kim, C. Kempen, J. Axelrad, H. Huang, S. Khalid, V. Shah, O. Eskiocak, O. B. Parks, A. Berisha, J. P. McAleer, M. Good, M. Hoshino, R. Blumberg, A. B. Bialkowska, S. L. Gaffen, J. K. Kolls, V. W. Yang, S. Beyaz, K. Cadwell, P. Kumar, en, *Immunity* **55**, 237–253.e8, ISSN: 1074-7613 (Feb. 2022).

Supplementary file consisting of figures S1-S9 and methods

BMP-signaling in the intestinal epithelium drives a critical feedback loop to restrain IL-13-driven tuft cell hyperplasia

Håvard T. Lindholm[1,+*], Naveen Parmar[1,+], Claire Drurey[2], Marta Campillo Poveda[2], Pia Vornewald[1], Jenny Ostrop[1], Alberto Díez-Sanchez[1], Rick M. Maizels[2], and Menno J. Oudhoff[1,*]

[1]CEMIR – Centre of Molecular Inflammation Research, Department of Clinical and Molecular Medicine, NTNU – Norwegian University of Science and Technology, 7491 Trondheim, Norway

[2]Wellcome Centre for Integrative Parasitology, Institute of Infection, Immunology and Inflammation, University of Glasgow, G12 8TA Glasgow, United Kingdom.

[+]these authors contributed equally to this work

[*]corresponding authors: havard.t.lindholm@ntnu.no and menno.oudhoff@ntnu.no

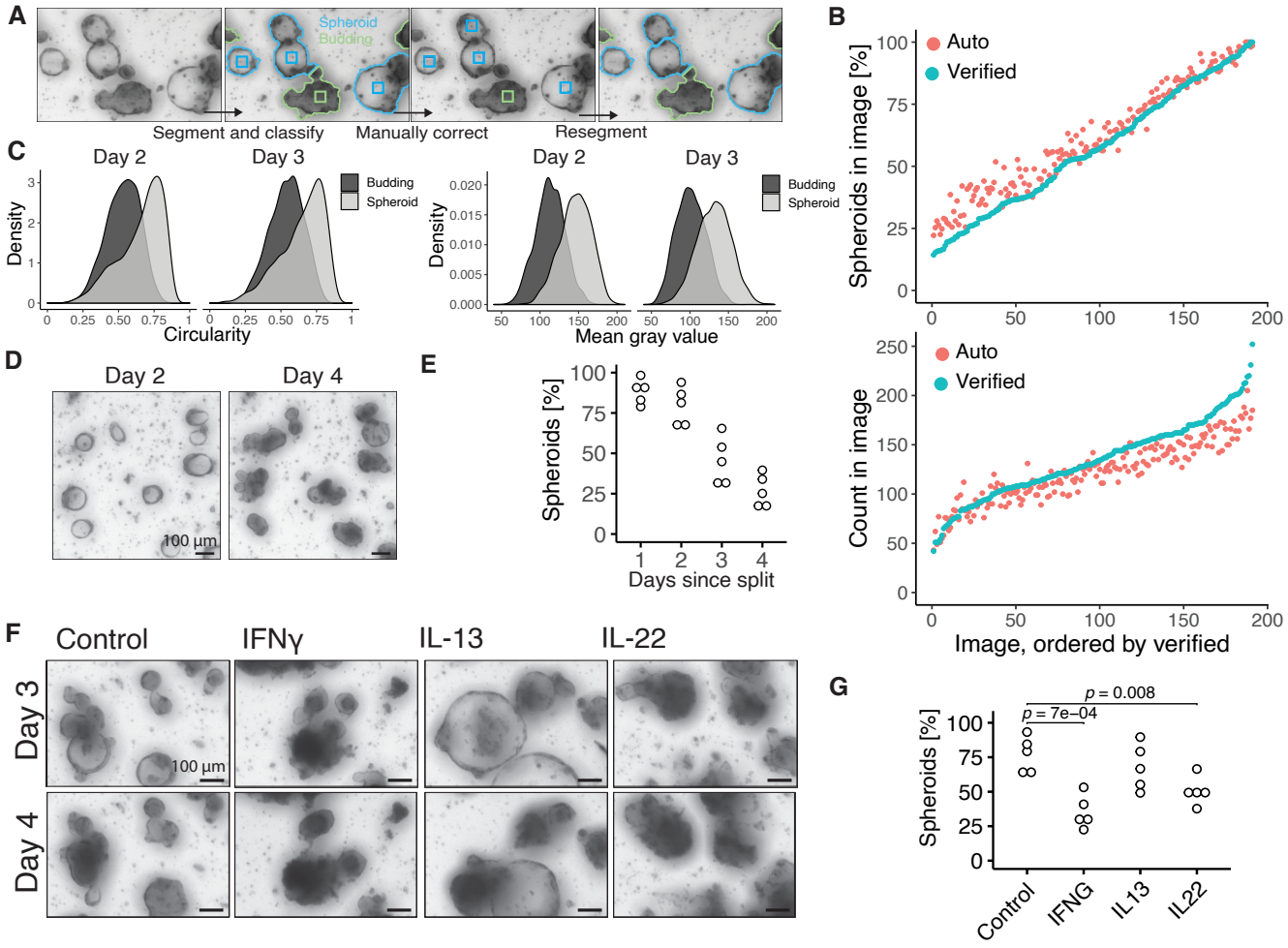

Figure S1: Image analysis pipeline. **A**, A segmentation algorithm is used to find the outline and center of an organoid and the segmented organoid is classified by a neural network. An optional manual correction of organoid centers and classification can be performed. The organoids can then be segmented again which gives an updated segmentation following the manual correction. **B**, Comparison of automatic segmentation and automatic classification of organoids compared to manually verified segmentation and manually verified classification. Each circle represents one image with approximately 100 organoids each. **C**, Distribution of circularity and mean gray value (higher value is whiter) of untreated small intestinal organoids. **D**, Representative images of untreated organoids. Media changed at day 2. **E**, Average fraction of spheroids in each image in same experiment as D. Each circle is one biological replicate and is the average of at least 3 images and in total this plot represents 16,462 organoids. **F**, Minimal projections of small intestinal organoids treated with cytokines. Days since seeding. **G**, Average fraction of spheroids at day 2 since splitting. Each circle is one biological replicate and is the average of at least 3 images and in total represents 10,462 organoids. P-values calculated with unpaired two-tailed T-test.

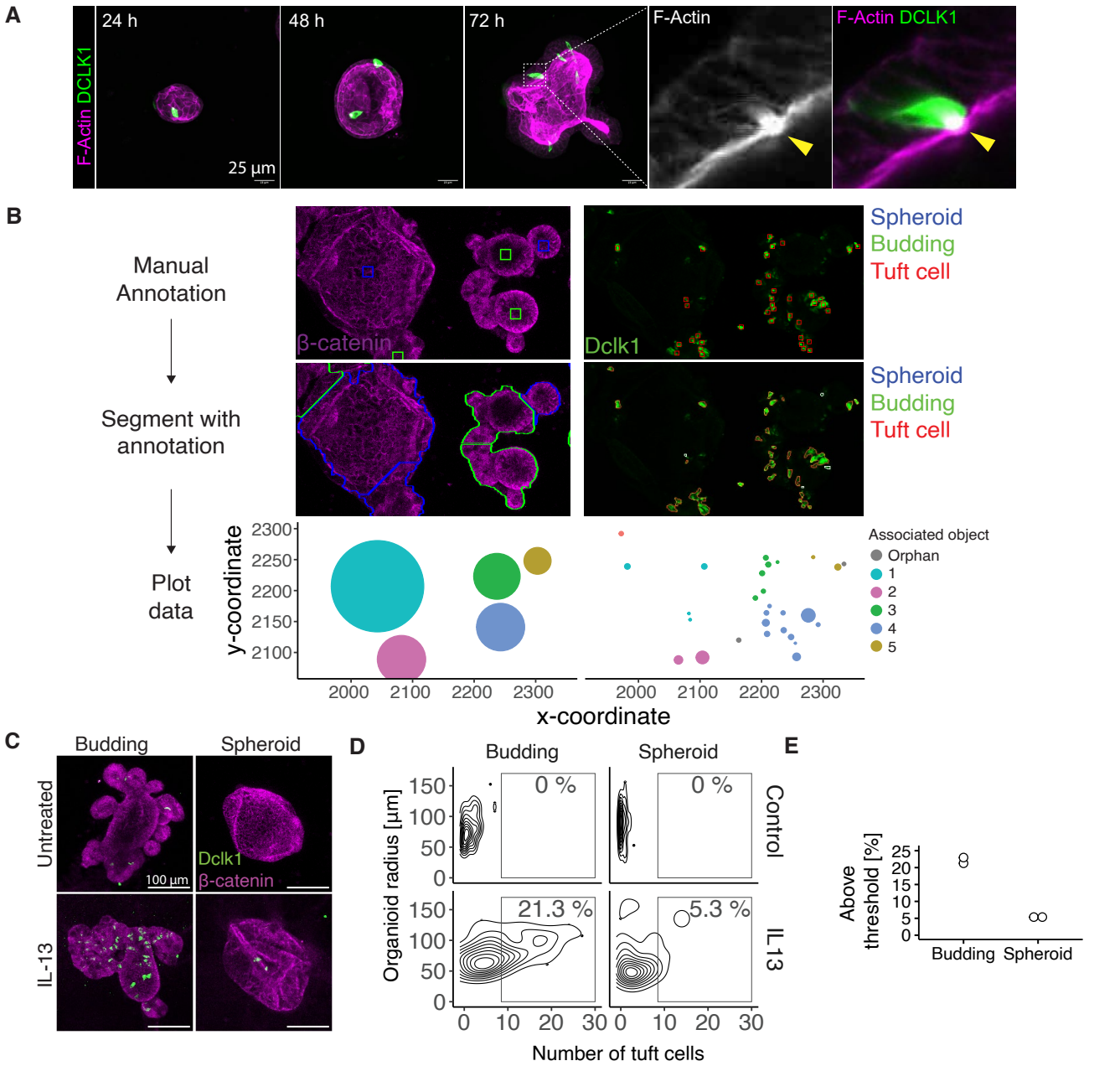

Figure S2: Quantification of number of tuft cells in organoids. **A**, Time course of tuft cell development in organoids. Times are hours since seeding. **B**, Image output from each step in the confocal image analysis pipeline. The center of each object of interest is marked with a square in a custom graphical user interface, and this information is used to separate overlapping objects. Furthermore, objects in other channels, like tuft cells, are analyzed to map which organoid they are inside. This information is summarized and used to plot number of tuft cells per organoid. **C**, Representative confocal images of small intestinal organoids at day 3 since splitting. **D**, Quantification of images shown in C. Percentages are relative to total number of organoids in that treatment. Plot shows the distribution of 192 organoids. **E**, Percentages for IL-13 treated organoids calculated as shown in D. Each circle is one biological replicate. All images in this figure are projections of Z-stacks.

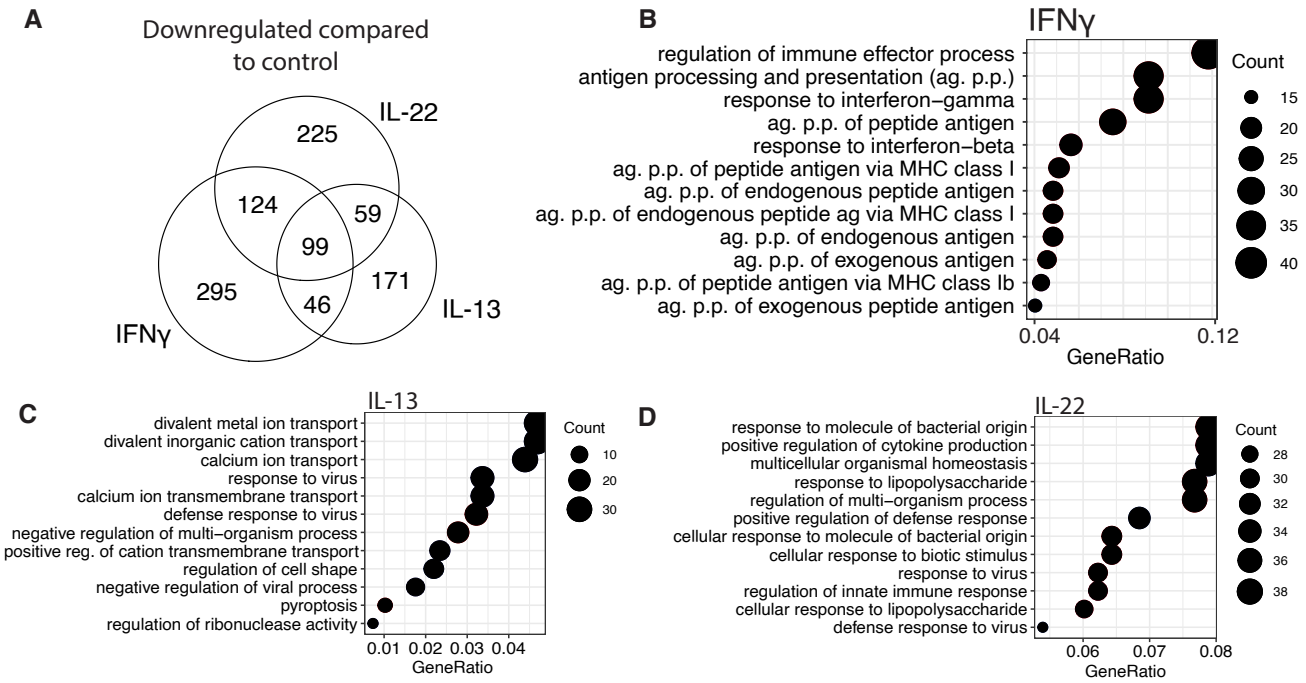

Figure S3: Details of RNA sequencing data of cytokines. **A**, Number of down-regulated significant genes from small intestinal organoids treated with indicated cytokine for 24 hours compared to control ($p<0.05$ and log2fc $<$ -1). **B-D**, Top hits from GO-term analysis of "biological process" in RNAseq data from intestinal organoids treated with indicated cytokine for 24 hours compared to control.

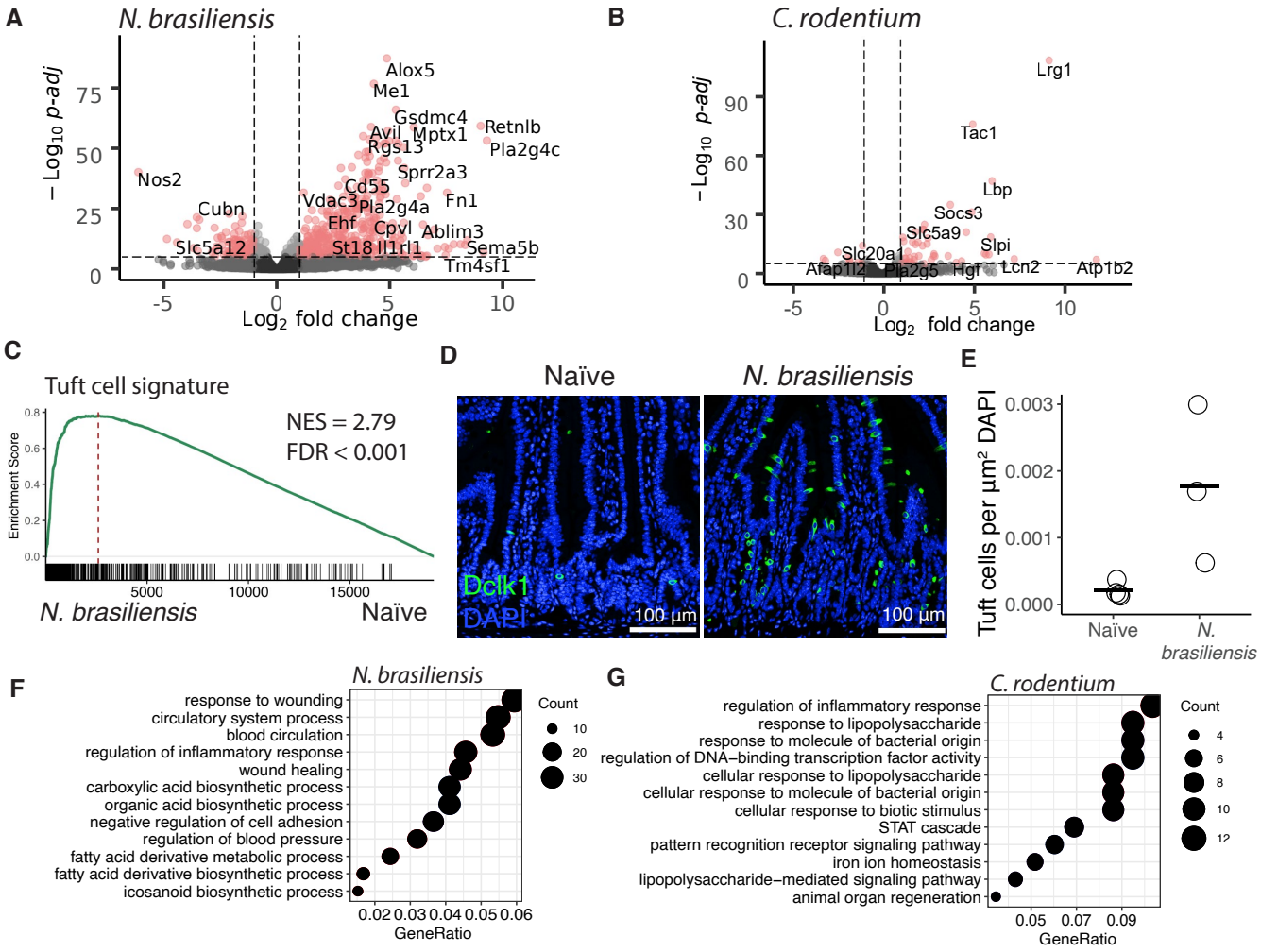

Figure S4: **A**, Volcano plot of RNAseq from intestinal epithelial tissue extracted from duodenum from mice seven days after infection with *N. brasiliensis*. **B**, Volcano plot of RNAseq from intestinal epithelial tissue extracted from colon from mice six days after infection with *C. rodentium*. **C**, GSEA analysis of a tuft cell signature on mRNA data from intestinal epithelium from *N. brasiliensis* infected mice. **D**, Confocal microscopy of cross section of mouse intestine seven days after infection with *N. brasiliensis* and naïve. **E**, Automatic tuft cell count from same experiment as D. Each circle represents quantitation from one full cross section from one mouse. **F**, **G**, Top hits from GO-term analysis of "biological process" in RNAseq data from mouse intestine infected with indicated pathogen.

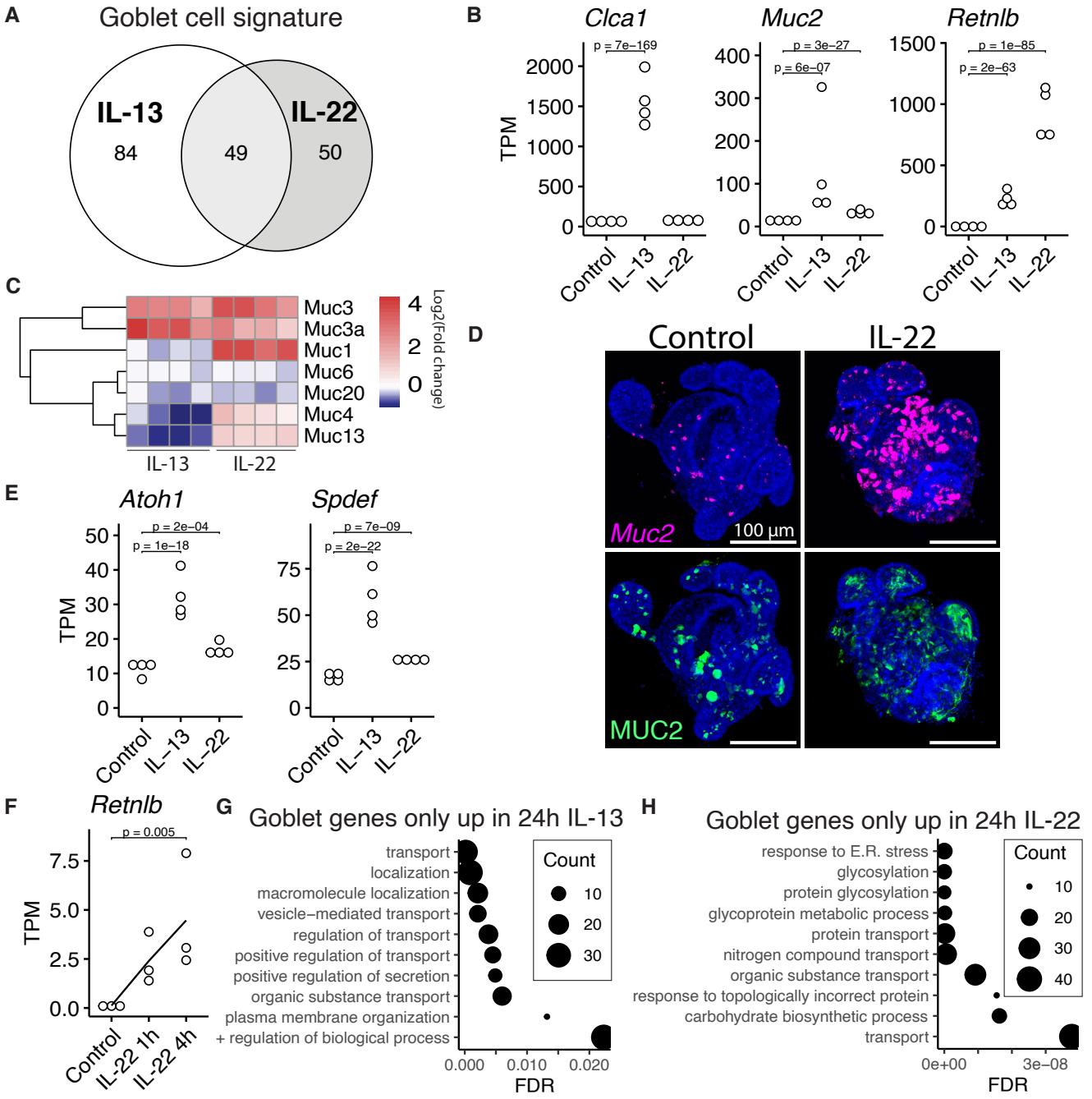

Figure S5: IL-13 and IL-22 gives different goblet cells also after 72 hours of cytokine stimulation. **A**, Distribution of how the plate based scRNAseq goblet cell gene set from Haber et al is changed upon 72 hours of IL-13 and IL-22 treatment. Up is defined as lg2fc>0.5 and p-adj<0.05. **B**, Gene expression from intestinal organoids treated for 72 hours with indicated cytokine. Each circle is one biological replicate. Statistics calculated with DESeq2, see methods. **C**, Expression of mucins in intestinal organoids stimulated IL-13 or IL-22 for 24 hours compared to control. **D**, Confocal imaging of organoids stained with an antibody staining for MUC2 in green and RNAscope probe for *Muc2* in purple. Organoids were imaged 3 days after seeding and 5 ng/mL of IL-22 was used since day of seeding. **E**, See B. **F**, Gene expression from intestinal organoids treated for 1 and 4 hours with IL-22. Each circle is one biological replicate. Statistics calculated with DESeq2, see methods. **G**,**H**, GO terms associated with gene sets seen in venndiagram in figure 2B. FDR = False discovery rate.

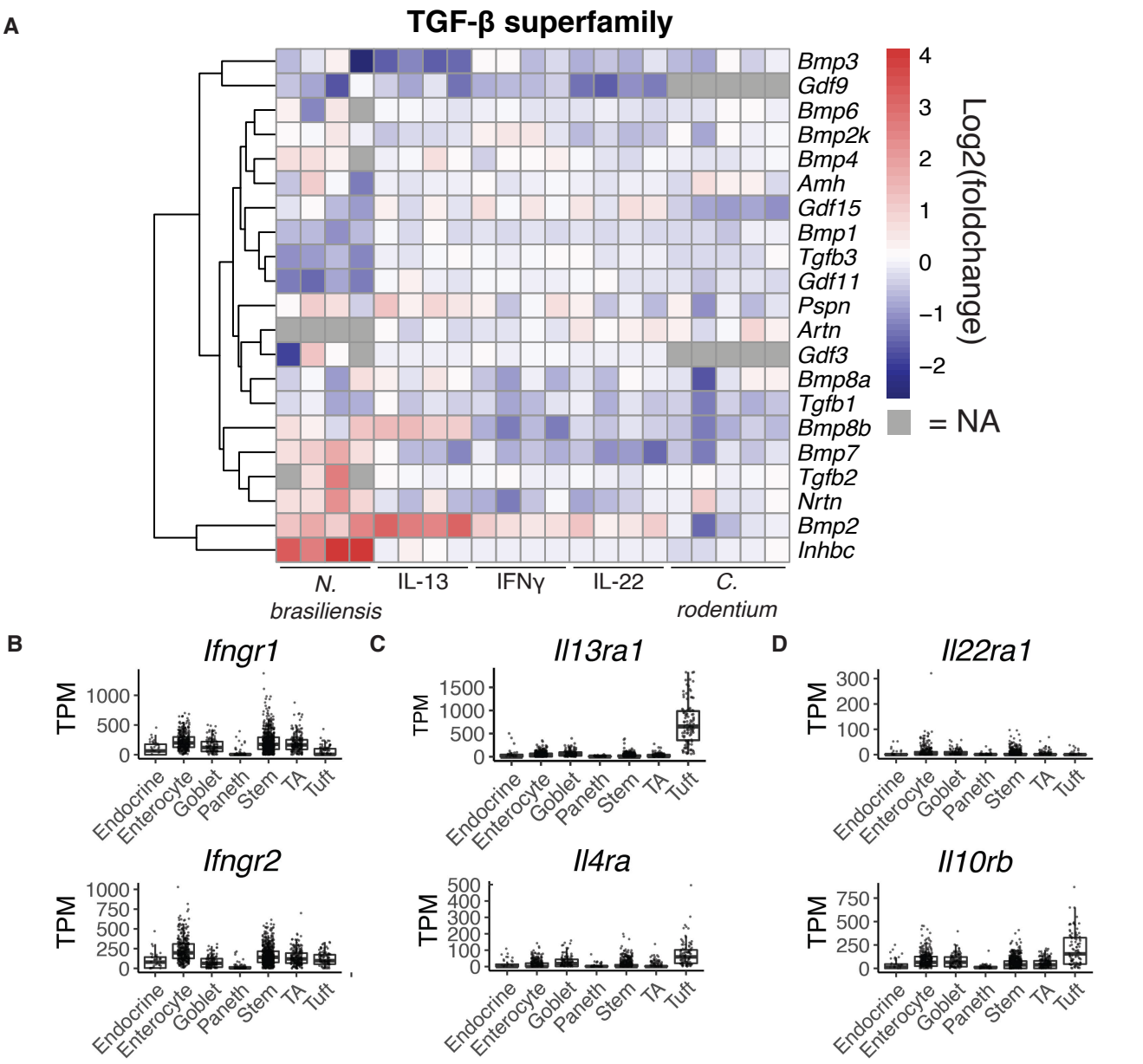

Figure S6: *Bmp2* is the main TGF-β superfamily member induced by IL-13. **A**, Heatmap of log2 fold change for TGF-β superfamily members from mRNAseq data from intestinal epithelium from mice infected with *N. brasiliensis* or *C. rodentium* and organoids treated for 24 hours with indicated cytokine. **B-D**, Expression of cytokine receptors, for IFNγ (B), IL-13 (C) and IL-22 (D), from plate based scRNAseq from Haber et al (*1*). TA = Transit amplifying.

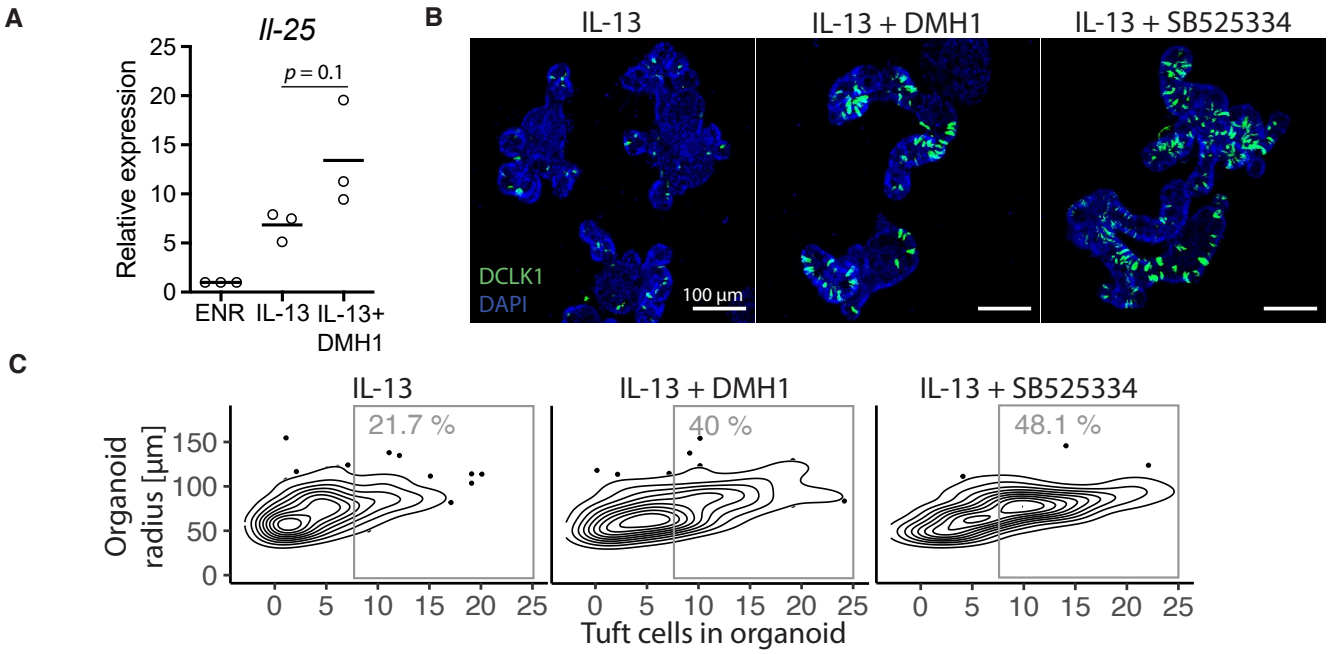

Figure S7: The effect of SB525334 on IL-13 dependent tuft cell hyperplasia. **A**, Relative expression of *Il-25* in intestinal organoids treated with indicated treatment for 72 hours determined with qPCR. p-value is calculated with unpaired two tailed T-test. **B**, Confocal staining of DCLK1 in small intestinal organoids treated with indicated treatments for 72 hours. **C**, Automatic quantification of same experiment as B. Each dot is one organoid.

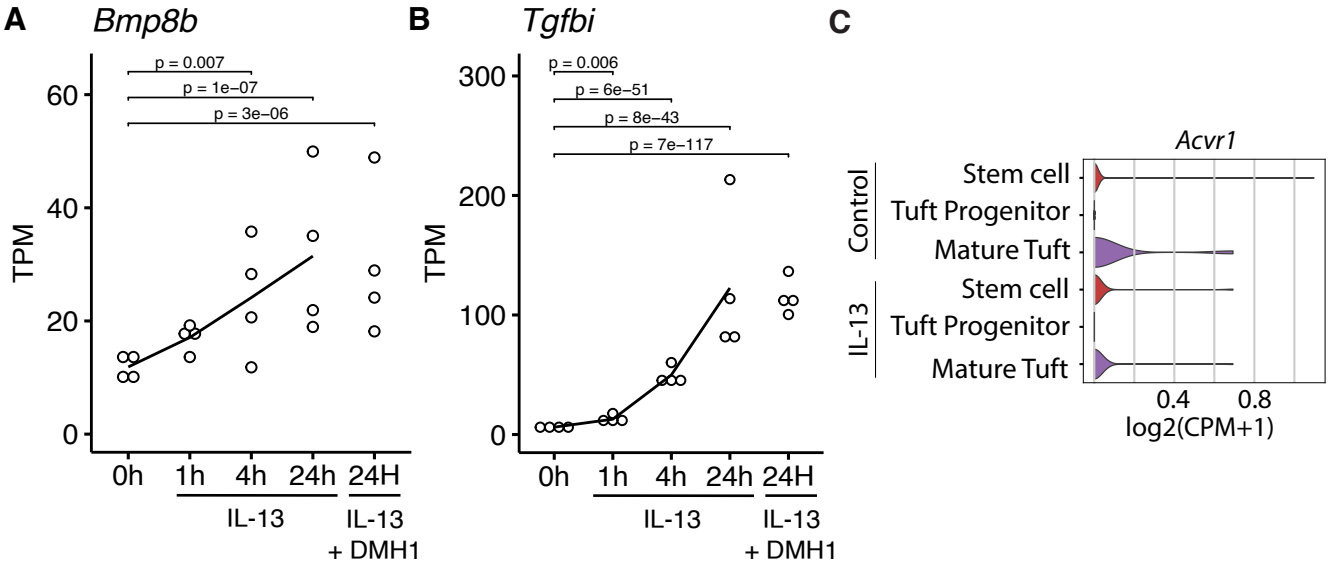

Figure S8: Time course of *BMP8b* and *Tgfbi* expression. **A**,**B**, Time points for RNAseq experiment from small intestinal organoids treated with 10 ng/mL IL-13 at indicated timepoints and with and without 5 µM DMH1 for 24 hours. Each circle is one biological replicate, statistics calculated with DEseq2, see methods. **C**, Violin plots of gene expression from scRNAseq data of small intestinal organoids treated with IL-13 and untreated from Biton et al (*2*).

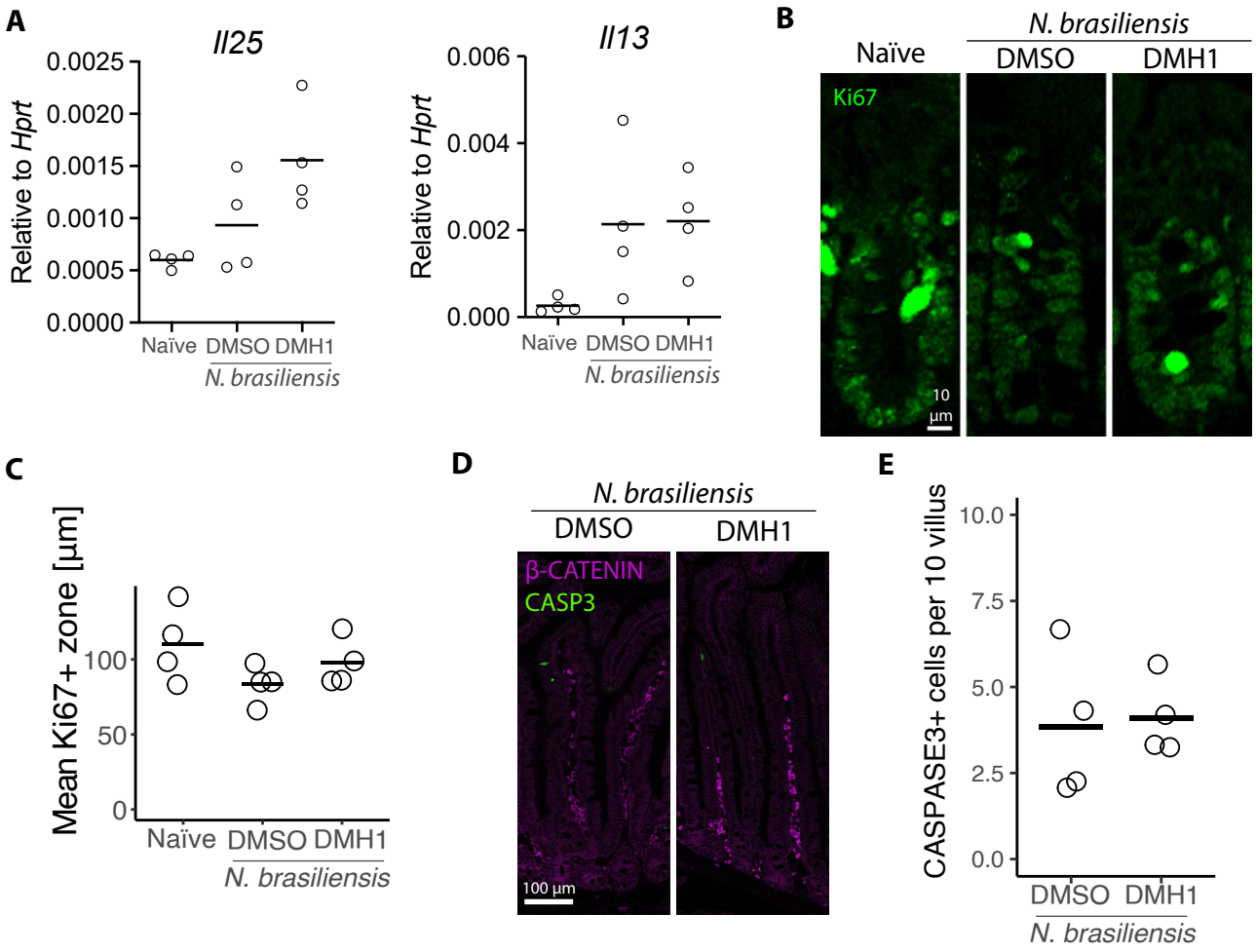

Figure S9: Further characterization of mice treated with DMH1 and DMSO and infected with *N. brasiliensis*. **A**, qPCR of indicated gene in duodenal intestinal tissue after 8 days of infection with *N. brasiliensis*. **B**, Ki67 staining in duodenal crypts from mice after 8 days of infection with *N. brasiliensis*. **C**, Quantification of height of Ki67+ zone in images shown in B. Each dot is the average of at least 5 crypts in one mouse. **D**, Staining of cleaved Caspase3 in duodenal crypt and villus from mice after 8 days of infection with *N. brasiliensis*. **E**, Manual quantification of images shown in D. Each circle is the average of at least 20 villus in one mouse.

Methods

Animal experiments

All mouse work done in Norway was performed in accordance with CoMed NTNU institutional guidelines and Norwegian legislation on animal experiments. Mice were handled under pathogen-free conditions. The C57BL/6 mice strain was used for all experiments.

The mice studies for *Citrobacter rodentium* infection were approved by Norwegian Food Safety Authority (FOTS ID: 11842). Briefly, C. rodentium was grown at 37 °C in Luria- Bertani (LB) medium supplemented with chloramphenicol (30 µg/ml) overnight. 9-11 weeks old mice were orally gavaged with a culture of 10^8 – 10^9 CFU per mouse delivered in a volume of 100 µL of sterile PBS. Mice remained infected with *C. rodentium* for six days. To determine the infection level, fecal samples were collected on day 5, homogenized in sterile PBS with a FastPrep homogenizer. After serial dilution of fecal samples, homogenates were plated on chloramphenicol resistant agar plates and the plates were counted after 24 h of growth at 37 °C. After 6 days of infection, mice were euthanized by CO_2 inhalation, parts of distal colon tissue was harvested for isolation of crypts as described below. RNA was isolated and samples were further used for RNAseq analysis.

Mice studies with *Nippostrongylus brasiliensis* infection used mice aged 8-12 weeks maintained in individually ventilated cages according to UK Home Office guidelines. *N. brasiliensis* was maintained as previously described (*3*). Mice were infected with larva of *N. brasiliensis* subcutaneously. 200 L3 larvae was used for sequencing experiments and 400 L3 larvae was used for experiments with DMH1. For experiments with DMH1, 4 mg/kg DMH1 dissolved in 20 µL DMSO, or control of DMSO alone, was administrated every other day, starting one day before infection. Mice were euthanized via cervical dislocation, and duodenal tissue harvested to use in imaging and for isolation of crypts as described below.

Small intestine and colon crypt isolation

Crypts from small intestine and colon where isolated according to a published protocol (*4*). In summary, the duodenal small intestine (first 10 cm from end of stomach) or distal colon of mouse was washed in ice-cold PBS and opened longitudinally. A microscopy cover slip was used to gently scrape of excess mucus and villus before the intestine was cut into 2-4 mm pieces. The fragments were resuspended in 30 mL ice-cold PBS and pipetted up and down with a 10 mL pipette. Supernatant was discarded and this step was repeated 5-10 times until the supernatant was clear. The fragments were incubated in 2 mM EDTA in PBS for small intestine, and 10 mM EDTA in PBS for colon, at 4 °C for 30 min with gentle rocking. The supernatant was removed, 20 mL of ice-cold PBS was added and the fragments were pipetted up and down. This washing step was repeated until the crypt fraction appeared as seen in a microscope. The 1-3 consecutive crypt fractions were passed through a 70 µm cell strainer and collected into a FCS coated 50 mL tube. The crypts were spun down at 300 x*g* for 5 min and washed once in 10 mL ice cold PBS at 200 x*g* for 5 min.

Small intestinal organoid culture

Approximately 200-500 crypts were resuspended in 50 µL Matrigel (Corning, 734-1101) and kept at 4 °C. 50 µL of the Matrigel solution was added to the center of a pre-warmed 24 well plate or 8-well microscopy slide (Ibidi, 80821) and quickly transferred to an incubator at 37 degrees with 5 % CO_2. After 5 min the pellet had solidified and 500 µL of basal culture medium was added and the plate was put back into the incubator. Basal culture medium consisted of advanced Dulbecco's modified Eagle medium - F12 supplemented with penicillin/streptomycin, 10 mM HEPES, 2 mM Glutamax, 1x N2 [ThermoFisher Scientific 100X, 17502048], 1x B-27 [ThermoFisher Scientific 50X, 17504044], and 1x N-acetyl-L-cysteine [Sigma, A7250]) and overlaid with ENR factors containing 50 ng/ml of murine EGF [Thermo Fisher Scientific, PMG8041], 20 % condition medium (CM) from a cell line producing R-Spondin (kind gift from Calvin Kuo, Stanford University School of Medicine, Stanford, CA, USA) and 10 % Noggin-CM (a kind gift from Hans Clevers, Hubrecht

Institute, Utrecht, The Netherlands). The culture medium was replaced every 2-3 days. Organoids were passaged by disrupting them with strong mechanical pipetting, letting the solution cool on ice before centrifuging at 200 xg, 5 min at 4 °C and resuspending in Matrigel. Organoid lines were maintained and normal budding morphology was observed throughout passaging. All experiments have been done within the range of 4-50 passaging events.

ELISA

BMP2 ELISA

qPCR

qPCR of intestinal organoids treated with IL-13 + DMH1 and nippo RNAlater tissue

Bright field imaging and quantification of intestinal organoids

Z-stacks covering the entire Matrigel droplet were captured using a EVOS2 microscope with CO_2, temperature and a humidity-controlled incubation chamber (Thermo-Fisher Scientific). 2D morphological properties of organoid objects as well as their classification were gathered using a custom analysis program written in python based on opencv2 (*5*). The brightness of images were autoscaled to max brightness, and a canny edge detection algorithm was run on each individual z-plane using the opencv2.canny function. Groups of pixels below a certain size was removed and a minimal projection of the edges was generated. This image was used to define the contour of objects. The implementation of opencv2s wathershed algorithm was used to split somewhat overlapping objects from each other and the center of the object was defined as the pixel furthest from the edge of the object. Each defined object contour was used to extract a 120x120 pixel picture of the object on a white background from a minimal projection of the original z-stack. These images were used to classify the organoid as either "Junk", "Budding" or "Spheroid" with a convolutional neural network implemented using Tensorflow and Keras (*6*, *7*). The network

was trained on about 25 000 manually classified 120x120 images prepared as just described. For initial analysis these data were plotted, but for plots used in this publication the pictures were reviewed manually in a graphical user interface (GUI) written in python. This GUI displayed the center of each object and its classification and enabled addition of new object centers or editing of automatically found object centers. The manually verified annotations were used to re-run the segmentation as described above, but this time the classification of the objects were not changed and a watershed algorithm were used to segment object contours based on the manually curated object centers. Finally, objects with a size less than 300 pixels were filtered out. To highlight differences between treatments, thresholds for percentage calculations were generally chosen to be set around the upper bound of the treatment with the lowest organoid radius. Plots were made with the R-package ggplot2 (*8*).

Immunofluorescence staining of organoids and imaging

The Matrigel used for organoids grown for immunofluorescent imaging were cultured in Matrigel mixed with 25 % basal culture medium (described above) in eight-well slides (Ibidi, 80821). Media was removed and organoids were fixed in 300 µL 4% PFA with 2 % sucrose for 30 minutes. Fixation solution was removed and 300 µL PBS was added, after 5 minutes the PBS was removed. This washing step was done a total of two times. The PBS was removed and 0.2% Triton X-100 in PBS was added for 30 minutes at room temperature to permeabilize the cell membranes. The wells were then washed in PBS, 3 times, 5 minutes each time. Free aldehydes were blocked in 100 mM Glycine for 1 hour at room temperature and thereafter the wells were incubated in 300 µL blocking buffer (2 % normal goat serum, 1 % BSA and 0.2 % Triton X-100 in PBS) for 1 hour at room temperature. Primary antibodies, β-catenin (1:200, mouse mAb, Santa Cruz Biotechnology, sc-7963), DCLK1 (1:250, rabbit pAb, abcam, ab31704), MUC2 (1:200, rabbit pAb, Santa Cruz Biotechnology sc-15334) and RELM-β (1:200, rabbit pAb, PeproTech 500-P215) were diluted in 150 µL blocking buffer and incubated overnight at 4 °C. The next day samples were washed in PBS with agitation, 3 times 10 minutes each time. The appropiate Alexa fluor Secondary antibody

(1:500), and DAPI (1:10 000) and UEA1 (Ulex Europaeus Agglutinin I Rhodamine-labeled Dil 1:500, Vector laboratories RL1062) was added in blocking buffer (1 % normal goat serum, 0.5 % BSA and 0.2 % Triton X-100 in PBS) and incubated at 4 °C with agitation over night. The next day the samples were washed in PBS, 3 times 5 minutes each time, and 250 µL Fluoromount G medium (ThermoFisher Scientific, 00-4958-02) was added to the well. Z-stacks of tile-scans covering the entire well were acquired on a Zeiss Airyscan confocal microscope using a 10X objective lens.

Immunofluorescence staining of tissue sections and imaging

The harvested intestinal tissue was fixed with 10% formalin for 48 h at room temperature. Tissue was subsequently dehydrated through a series of graded ethanol and then embedded in paraffin wax blocks. 5 µm thick sections were cut using a microtome, floated in a 40 °C water bath and transferred to a glass slide. After drying, the tissue sections were kept in an oven at 60 °C for 30 minutes and deparaffinized in two changes of Neo-clear (Xylene substitute) for 5 min each, followed by graded ethanol (100 % ethanol 2 times with 3 min each, and next transfer once through 95 %, 80 %, and 70 % ethanol and water 3 min each). Heat mediated antigen retrieval was performed using citrate buffer except for pSmad2 (phospho S255) where Tris/EDTA buffer pH 9 was used. Tissue sections on glass slides were marked with hydrophobic pen (PAP pen, ab2601) to keep staining reagents on the tissue section. Next, blocking buffer (1% BSA, 2% normal goat serum, 0.2% Triton X-100 in PBS) was added onto the sections of the slides and incubated in a humidified chamber at room temperature for 1 hour. Appropriately diluted primary antibody (antibody dilution buffer, e.g. 0.5 % bovine serum albumin, 1 % normal goat serum, 0.05 % Tween 20 in PBS) was added to the sections on the slides and incubate in a humidified chamber at 4 °C overnight. Primary antibodies used exclusively for tissue where Ki67 (1:100, rabbit mAb, invitrogen MA5-14520), pSMAD2 (phospho S255) (1:100, rabbit mAb, abcam ab188334), OLFM4 (1:100, rabbit mAb, Cell signaling 39141S). See organoid staining section for details of the other antibodies. The slides were washed in 0.2 % Triton X-100 10 min each. Next, secondary antibody conjugated with fluorochromes was added to the slides for 1 hour at room temperature in a humidified chamber.

DAPI and UEA1 was added to stain goblet cells. After rinsing three times with PBST (0.2 % Triton X-100 in PBS) for 10 min each, slides were mounted in Fluoromount G. Complete tile scans were acquired with a Zeiss Airyscan confocal microscope, using a 10x or 20x objective lens.

Combined RNA Scope and Immunofluorescence in organoids

Organoids were cultured in 8 Well Chamber, removable (IBIDI, Catalog no.80841) and ACD RNAScope protocol was followed with a few modifications. After treatments, media was removed, and 10 % neutral buffered formalin (NBF) was added to wells for 30 mins at room temperature (RT). NBF was decanted and organoids were washed with PBS two times. For dehydration, 1X PBS was removed and 50 % ethanol was added for 1 minute, followed by 70 % ethanol and then 100 % ethanol. For re-hydration, 70 % ethanol was added for 1 minute followed by 50 % ethanol for 1 minute at RT. Before beginning the RNA scope steps, a hybridization oven was set to 40° C. Chambers were carefully removed from the slides and organoid area was marked with a RNA scope hydrophobic pen. Next, RNAscope hydrogen peroxide solution was added to the wells for 10 minutes at RT and then removed. Wells were washed with fresh distilled water for two times. Then, two drops of protease III (1:15) was added to each well for 10 minutes at RT. Protease III solution was removed, and wells were washed twice with PBS for 2 minutes. Probes were warmed in incubator at 40° C for 10 minutes. Next, *Muc2* (ACD 315451-C3) probe (1: 100) was diluted in probe diluent (ACD 300041) and added to the wells for 2 hours in a hybridization oven kept at 40° C. After 2 hours, liquid was removed, and 1X wash buffer was added twice for 2 minutes. Next, 2 drops of RNAscope multiplex FL v2 Amp1 was added to each well for 30 minutes at 40° C in a hybridization oven. Wells were washed twice with 1X wash buffer. Next, RNAscope multiplex FL v2 Amp2 was added to the wells and incubated for 30 minutes at 40° C. Wells were washed twice with 1X wash buffer. After this, RNAscope multiplex FL v2 Amp3 was added to wells and incubated for 15 minutes at 40° C in a hybridization oven. After incubation, wells were washed twice with 1X wash buffer for 2 minutes. For *Muc2* probe, only HRP- C3 signal was developed. Next, 2 drops of RNAscope Multiplex FL v2 HRP-C3 was added to wells and incubated for 15

minutes at 40° C in a hybridization oven. Wells were washed twice with 1 x wash buffer for 2 minutes at RT. Next, Opal 690 (1:1000) diluted in TSA buffer was added to wells for 30 minutes at 40° C in a hybridization oven. Wells were washed twice with 1X wash buffer for 2 minutes at RT. Next, RNAscope Multiplex FL v2 HRP blocker was added to wells for 15 minutes at 40° C in a hybridization oven. Wells were washed twice with 1x wash buffer at RT. Next, 2 % Normal goat serum and 1 % BSA in PBS was added to wells for 30 minutes at RT. After this, RELMβ primary antibody (1: 200) and MUC2 primary antibody (1: 200) was added to wells overnight at 4° C in dark humidified chamber. Next day, wells were twice washed with PBS and anti-rabbit Alexa fluor 488 (1: 500), DAPI (1:1000) and UEA1-Rhodamine (1: 500) was added to wells overnight at 4° C in dark humidified chamber. Next day, solution was removed and washed twice with PBS. Slides were mounted with Fluoromount G and covered with cover slips. Images were acquired using Zeiss LSM 880 with a 20X objective.

RNA scope in tissue sections

RNA scope in tissue slides was performed according to RNAscope Multiplex Fluorescent V2 Assay manufactured by Advanced Cell Diagnostics. Briefly, the tissue slides were baked in a dry oven for one hour at 60° C. Next, paraffin was removed by incubating slides in Neoclear (xylene substitute) for 5 minutes twice at RT. After this, slides were incubated twice in 100 % ethanol for 2 minutes at RT. Then, hydrogen peroxide was added to the slides for 10 minutes at RT. Next, antigen retrieval was performed using 400 mL of 1X Target Retrieval reagents. Slides were kept in a beaker with boiling 1X Target Retrieval reagents on a hot plate heater for 15 minutes. Next, slides were transferred to a rinse container with distilled water and rinsed for 15 seconds. After that, slides were transferred to 100 % ethanol for 3 minutes. After drying, a barrier was created around the tissue using a hydrophobic barrier pen. Slides were stored at RT overnight. The next day, the hybridization oven was set at 40° C. RNAscope protease plus drops were added to cover the whole tissue, and slides were incubated at 40° C for 30 minutes. Slides were washed twice with distilled water. Sox4-C2 (471381-C2) probe was warmed at 40° C for 10 minutes in an incubator and then

cooled to RT. Next, 50 µL of *Sox4* probe (1:50) diluted in probe diluent was hybridized onto each tissue section by incubating slides at 40° C for 2 hours. Also, a few drops of negative control probe were added to the two separate slides to check the specificity. After 2 hours, slides were washed twice with 1X wash buffer for 2 minutes at RT. Next, a few drops of RNAscope Multiplex FLv2 Amp1 were added to each slide and incubated for 30 minutes at 40° C. Slides were removed and washed twice with 1X wash buffer for 2 minutes at RT. Next, slides were incubated with RNAscope Multiplex FLv2 Amp2 for 30 minutes at 40 ° C, and slides were washed with 1X wash buffer for 2 minutes at RT. Then, slides were incubated with a few drops of RNAscope Multiplex FLv2 Amp3 for 15 minutes at 40°C. Slides were washed twice with 1X wash buffer for 2 minutes at RT. Next, excess liquid was removed, and slides were incubated with RNAscope Multiplex FLv2 HRP-C2 in the oven for 15 minutes at 40° C. Slides were removed and washed twice with 1X wash buffer for 2 minutes at RT. Next, Opal-690 diluted (1:1000) in TSA buffer was added onto the slides in the oven for 30 minutes at 40°C and then washed twice with 1X wash buffer for 2 minutes at RT. Slides were further incubated with RNAscope Multiplex FLv2 HRP- blocker for 15 minutes at 40° C and then washed with 1X wash buffer at RT for 2 minutes. Slides were counter-stained with DAPI (1:1000) and mounted in Fluoromount G and covered with glass slides. 20X tile scan images were acquired using the ZEISS LSM880 microscope.

Quantification of immunofluorescence images

2D morphological properties of intestinal organoid objects in confocal images were gathered using a custom analysis program written in python based on opencv2 (*5*). Maximal projections of each channel were created as well as a rgb composite of all channels, hereafter referred to as the combined channel. The center position of all intestinal organoids as well as their class as either "budding" or "spheroid" were manually annotated in the combined channel using a custom graphical user interface. A binary threshold individual to each channel was then applied to create channel masks and additionally, these masks were added together to a combined mask. Contours of objects were defined based on the outline in combined mask and they were split using a watershed algorithm

where the manual annotations were used as input. Only objects in the combined channel with a manual annotation were kept for further analysis. 2D morphological properties such as area, perimeter and circularity of each object in the combined channel was acquired as well as the mean intensity of each channel. Furthermore, tuft cells were manually annotated in the DCLK1 channel using the custom graphical user interface. The number of tuft cells inside each object in the combined channel could therefore be counted. To highlight differences between treatments, thresholds for percentage calculations were generally chosen to be set around the upper bound of the treatment with the lowest induction in tuft cells. These data were processed in R and plotted with the ggplot2 package (*8*).

The same analysis were applied to confocal images of tissue staining with some changes. A binary mask defining the tissue area to quantify, for example crypts, villus or both, was manually made for each tissue section. Furthermore, manual annotation of tuft cells was done for a selection of images using a custom written graphical user interface. The number of manual tuft cells inside the manually made tissue section mask was counted. In addition, both the mean intensity of each channel and the number of pixels above a channel-individual threshold was measured for each channel inside each marked region in the tissue mask. This enabled a calculation of number of manually counted tuft cells per μm^2 DAPI positive pixel and quantification of fluorescence intensity per crypt. Furthermore, a binary threshold of the DCLK1 channel allowed definition of automatically defined tuft cell objects. Whether a DCLK1 object was a tuft cell or noise could be confirmed by checking for presence of a manual tuft cell annotation. In this way, gates for selecting tuft cells where defined and used for images that were not manually annotated. These data were processed in R and plotted with the ggplot2 package (*8*).

A similar approach was used to quantify *Bmp2* RNAscope signal in tuft cells compared to background. A mask was manually drawn around each *Dclk1* positive area approximately encompassing a single tuft cell. Another mask (called background) was drawn around the rest of the cells in the crypt without *Dclk1* signal. These masks were used in the same script as described in the previous paragraph, further processed in R, and plotted with the ggplot2 package (*8*)

RNA isolation and sequencing

RNA was extracted with Quick-RNA Microprep Kit according to the manufacturers instructions (Zymo, R1050). Library preparation and sequencing for 24 hour cytokine samples was performed by NTNU Genomic Core facility. Library preparation was done with Lexogen SENSE mRNA kit and the library was sequenced on two Illumina NS500 HO flowcells, 75 bP single stranded. All other library preparation and sequencing was performed by Novogene (UK) Co. using the NEB Next® Ultra™ RNA Library Prep Kit. Samples were sequenced at 150 bp paired end using a Novaseq 6000 (Illumina).

Batch RNA sequencing analysis

Reads were aligned to the *Mus Musculus* genome build mm10 using the STAR aligner (*9*). The count of reads that aligned to each exon region of a gene in GENCODE annotation M18 of the mouse genome (*10*) was counted using featureCounts (*11*). Genes with a total count less than 10 across all samples were filtered out. A differential expression analysis was done with the R-package DESeq2 (*12*), and volcano plots were plotted with the R-package EnhancedVolcano (*13*). PCA analysis was performed with the scikit-learn package with the function sklearn.decomposition.PCA (*14*). GSEA analysis was run with the log2(fold change) calculated by DESeq2 as weights, 10000 permutations and otherwise default settings using the R-package clusterProfiler (*15*). GO term analysis was run using the function enrichGO in clusterProfiler. The R-packages pheatmap and eulerr where used to make heatmaps and venndiagrams, respectively (*16*, *17*). RNAseq of organoids grown in the absence and presence of Noggin can be found from the ArrayExpress accession E-MTAB-9181 and analysed as described in (*18*).

Single cell RNA sequencing analysis

Barcodes, genes and matrix files for control and IL-13 treated samples were downloaded from GEO accession GSE106510 (*2*). Additionally, BAM files from GSE106510 were downloaded from

sequencing read archive (SRA) and velocyto was run on these data using mouse genome mm10 with repeatmask for mm10 (*19*, *20*). Matrix data and velocyto output were loaded into one adata object in scanpy (*21*). QC filtering was already perfomed on the matrix files and therefore, only cells with less than 500 genes detected and genes found in less than 20 cells were filtered out. Counts were normalized to log(count+1) using the natural logarithm. An UMAP was created with 50 PCA dimensions. Cell clusters were named based on comparison to Haber et als gene sets for cell types (*1*). Tuft cells where then selected and subgrouped into two clusters using the leiden algorithm with a resolution of 0.09. RNA velocity was calculated and plotted with scVelo (*22*).

Supplementary Tables

Supplementary file 1 - GSEA gene sets

All gene sets used for GSEA. See file *Supplementary_file_1_gsea.xlsx.*

Supplementary file 2 - Goblet cell gene signatures

Goblet cell genes from plate based scRNAseq compared to genes up-regulated in 24 hour treatment with IL-13 and IL-22. See file *Supplementary_file_3_goblet_cell_signatures.xlsx*

References

1. A. L. Haber, M. Biton, N. Rogel, R. H. Herbst, K. Shekhar, C. Smillie, G. Burgin, T. M. Delorey, M. R. Howitt, Y. Katz, I. Tirosh, S. Beyaz, D. Dionne, M. Zhang, R. Raychowdhury, W. S. Garrett, O. Rozenblatt-Rosen, H. N. Shi, O. Yilmaz, R. J. Xavier, A. Regev, en, *Nature* **551**, 333–339, ISSN: 0028-0836, 1476-4687 (Nov. 2017).

2. M. Biton, A. L. Haber, N. Rogel, G. Burgin, S. Beyaz, A. Schnell, O. Ashenberg, C.-W. Su, C. Smillie, K. Shekhar, Z. Chen, C. Wu, J. Ordovas-Montanes, D. Alvarez, R. H. Herbst, M. Zhang, I. Tirosh, D. Dionne, L. T. Nguyen, M. E. Xifaras, A. K. Shalek, U. H. von Andrian, D. B. Graham, O. Rozenblatt-Rosen, H. N. Shi, V. Kuchroo, O. H. Yilmaz, A. Regev, R. J. Xavier, en, *Cell* **175**, 1307–1320.e22, ISSN: 00928674 (Nov. 2018).

3. M. Camberis, G. Le Gros, J. Urban, eng, *Current Protocols in Immunology* **Chapter 19**, Unit 19.12, ISSN: 1934-368X (Aug. 2003).

4. T. Sato, H. Clevers, en, in *Epithelial Cell Culture Protocols: Second Edition*, ed. by S. H. Randell, M. L. Fulcher (Humana Press, Totowa, NJ, 2013), pp. 319–328, ISBN: 978-1-62703-125-7.

5. G. Bradski, *The OpenCV Library*, Library Catalog: www.drdobbs.com, 2000, (`http://www.drdobbs.com/open-source/the-opencv-library/184404319`).

6. M. Abadi, A. Agarwal, P. Barham, E. Brevdo, Z. Chen, C. Citro, G. S. Corrado, A. Davis, J. Dean, M. Devin, S. Ghemawat, I. Goodfellow, A. Harp, G. Irving, M. Isard, Y. Jia, R. Jozefowicz, L. Kaiser, M. Kudlur, J. Levenberg, D. Mane, R. Monga, S. Moore, D. Murray, C. Olah, M. Schuster, J. Shlens, B. Steiner, I. Sutskever, K. Talwar, P. Tucker, V. Vanhoucke, V. Vasudevan, F. Viegas, O. Vinyals, P. Warden, M. Wattenberg, M. Wicke, Y. Yu, X. Zheng, *arXiv* (2015).

7. *Keras*, 2015, (`https://keras.io/`).

8. H. Wickham, *ggplot2: Elegant Graphics for Data Analysis* (Springer-Verlag New York, 2016), ISBN: 978-3-319-24277-4.

9. A. Dobin, C. A. Davis, F. Schlesinger, J. Drenkow, C. Zaleski, S. Jha, P. Batut, M. Chaisson, T. R. Gingeras, en, *Bioinformatics* **29**, 15–21, ISSN: 1367-4803 (Jan. 2013).

10. A. Frankish, M. Diekhans, A.-M. Ferreira, R. Johnson, I. Jungreis, J. Loveland, J. M. Mudge, C. Sisu, J. Wright, J. Armstrong, I. Barnes, A. Berry, A. Bignell, S. Carbonell Sala, J. Chrast, F. Cunningham, T. Di Domenico, S. Donaldson, I. T. Fiddes, C. García Girón, J. M. Gonzalez,

T. Grego, M. Hardy, T. Hourlier, T. Hunt, O. G. Izuogu, J. Lagarde, F. J. Martin, L. Martínez, S. Mohanan, P. Muir, F. C. P. Navarro, A. Parker, B. Pei, F. Pozo, M. Ruffier, B. M. Schmitt, E. Stapleton, M.-M. Suner, I. Sycheva, B. Uszczynska-Ratajczak, J. Xu, A. Yates, D. Zerbino, Y. Zhang, B. Aken, J. S. Choudhary, M. Gerstein, R. Guigó, T. J. P. Hubbard, M. Kellis, B. Paten, A. Reymond, M. L. Tress, P. Flicek, en, *Nucleic Acids Research* **47**, D766–D773, ISSN: 0305-1048 (Jan. 2019).

11. Y. Liao, G. K. Smyth, W. Shi, en, *Bioinformatics* **30**, 923–930, ISSN: 1367-4803 (Apr. 2014).

12. M. I. Love, W. Huber, S. Anders, *Genome Biology* **15**, 550, ISSN: 1474-760X (Dec. 2014).

13. K. Blighe, *Publication-ready volcano plots with enhanced colouring and labeling: kevinblighe/EnhancedVolc* original-date: 2018-02-16T13:36:36Z, Feb. 2019, (`https://github.com/kevinblighe/EnhancedVolcano`).

14. F. Pedregosa, G. Varoquaux, A. Gramfort, V. Michel, B. Thirion, O. Grisel, M. Blondel, P. Prettenhofer, R. Weiss, V. Dubourg, J. Vanderplas, A. Passos, D. Cournapeau, en, *MACHINE LEARNING IN PYTHON*, 6 (2011).

15. G. Yu, L.-G. Wang, Y. Han, Q.-Y. He, *OMICS: A Journal of Integrative Biology* **16**, 284–287 (Mar. 2012).

16. R. Kolde, *pheatmap: Pretty Heatmaps*, 2019, (`https://CRAN.R-project.org/package=pheatmap`).

17. J. Larsson, *eulerr: Area-Proportional Euler and Venn Diagrams with Ellipses*, 2019, (`https://cran.r-project.org/package=eulerr`).

18. M. M. Alonso, H. Lindholm, S. Iqbal, P. Vornewald, S. Hoel, M. Altelaar, P. Katajisto, A. Arroyo, M. Oudhoff, *bioRxiv* (2020).

19. G. La Manno, R. Soldatov, A. Zeisel, E. Braun, H. Hochgerner, V. Petukhov, K. Lidschreiber, M. E. Kastriti, P. Lönnerberg, A. Furlan, J. Fan, L. E. Borm, Z. Liu, D. van Bruggen, J. Guo, X. He, R. Barker, E. Sundström, G. Castelo-Branco, P. Cramer, I. Adameyko, S. Linnarsson, P. V. Kharchenko, en, *Nature* **560**, Bandiera_abtest: a Cg_type: Nature Research Journals

Number: 7719 Primary_atype: Research Publisher: Nature Publishing Group Subject_term: Differentiation;Genome informatics Subject_term_id: differentiation;genome-informatics, 494–498, ISSN: 1476-4687 (Aug. 2018).

20. W. Bao, K. K. Kojima, O. Kohany, *Mobile DNA* **6**, 11, ISSN: 1759-8753 (June 2015).

21. F. A. Wolf, P. Angerer, F. J. Theis, *Genome Biology* **19**, 15, ISSN: 1474-760X (Feb. 2018).

22. V. Bergen, M. Lange, S. Peidli, F. A. Wolf, F. J. Theis, en, *Nature Biotechnology* **38**, 1408–1414, ISSN: 1087-0156, 1546-1696 (Dec. 2020).